Master-Thesis

submitted in partial fulfillment of the requirements
for the degree of Master of Science

Hot electron emission from metallic nanoparticles

Author: Anton Hörl
Supervisor: Ao.Univ.-Prof. Mag. Dr. Ulrich Hohenester

University of Graz
Institute of Physics
Department of Theoretical Physics

November 26, 2012

Contents

1. Summary

Surface plasmons allow to bridge between the micrometer and nanometer length scales of optics and nanodevices. This is accomplished by converting light to coherent electron oscillations confined to the surface of nanostructures and leads to additional evenascent fields.

Of special interest are so-called hot spots that are regions with strong field enhancement with only a few nanometers dimensions caused by the surface plasmons situated e.g. at the edges and corners of a rectangular particle or in the feedgap region of bowtie antennas. Recently, it has been shown that such hot spots even with only small field enhancements [19] and surface plasmons [7] serve as emitters of hot electrons.

In this thesis hot-electron emission is investigated for different particle shapes - rectangular particles and bowtie antennas - and dimensions. We simulate the escaping electrons using the so-called simple man model [4, 7], where the electric fields are computed using the MNPBEM-Toolbox for plasmonic nanoparticles [15], and compare the results with measured electron spectra from lithographically fabricated gold nanoparticles, excited by femtosecond laser pulses.

The simulations reveal pronounced differences between different particle shapes. In particular, we observe higher excess energies at the same excitation intensity for bowtie antennas in comparison with rectangular particles. In addition we find that the main sources of electron emission and high kinetic energy electrons are the corners and edges of the particles. The higher excess energies of bowtie antennas are attributed to the feedgap region, where the field strength is enhanced in comparison to single rectangular particles. We also find good agreement between our simulation results and the experimental data.

2. Introduction

Metallic nanoparticles have a size in the nanometer range, at least in one dimension. Typically, the particles under study are about 20 to 200 nm in size, and have shapes of spheres, rectangular particles, or other geometries. These particles are interesting because light can couple to the free electrons in the conduction band of the metal and lead, under specific resonance conditions (depending on the dimensions and materials of the nanoparticles), to electron charge oscillations which are usually termed surface plasmons. Surface plasmons come together with so-called evenascent (exponentially decaying) electric fields with a strong field enhancement. Various applications in different fields, including medicine, sensor technology, optoelectronics, or photovoltaics are currently subject of intensive research [2].

Due to this highly localized fields, electrons can become photoexcited (either in multi-photon process or through quantum-mechanical tunneling) and accelerated in the evenascent fields, finally reaching high kinetic energies. Such electrons from metallic nanostructures with a small field enhancement have already been observed by various authors. Krüger et. al. [19] measured the generation of hot electrons from a tungsten tip excited by attosecond-laser pulses. They showed a dependence of the measured kinetic electron energies on the carrier-envelope phase of the laser [19] and also above-threshold photoemission [28]. Dombi et. al. [7] observed hot electron emission from metal films generated by surface plasmons. Furthermore, dependence of the measured kinetic electron energies on the carrier-envelope phase of the laser pulse [19] and above-threshold photoemission [28] was reported. In a recent work the group of Ropers [13] measured wavelength dependent kinetic electron energies from nanotips.

In this thesis we simulate electrons from fully plasmonic nanoparticles with field enhancements up to a factor 110 and compare them with experimental results obtained in the group of Peter Dombi in Budapest. Figure 2.1 shows the main processes of the system under study: upon excitation with a lin-

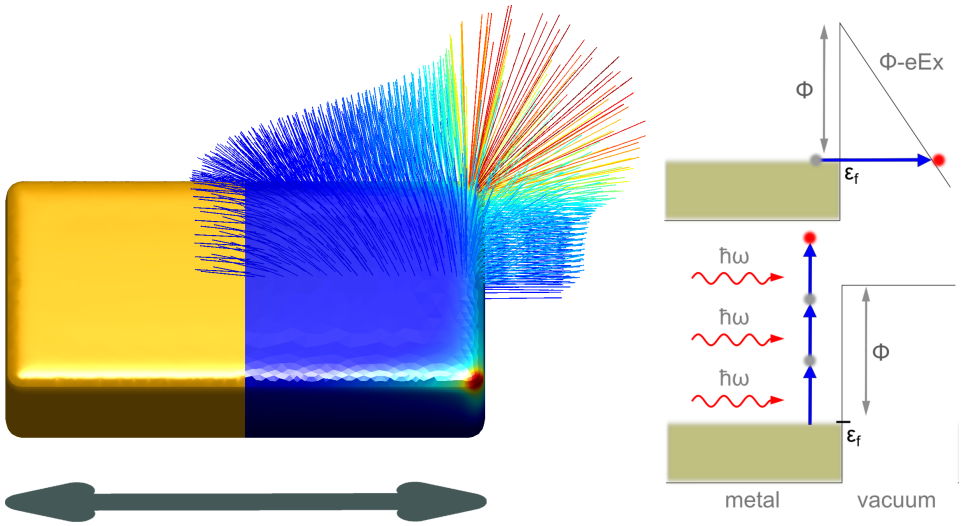

Figure 2.1.: Schematics of hot electron emission from metallic nanoparticles. Lines pointing away from the nanoparticle show the electron trajectories of the photon-emitted electrons, the colors correspond to their final kinetic energies. The gray arrow points in the direction of the linear polarized electric field. Electrons either absorb enough photons to overcome the barrier or tunnel through the barrier when the field strength strongly bends the potential.

early polarized femtosecond pulse, collective oscillations of the free electron gas of the gold nanoparticle (surface plasmons) are generated. Then electrons are emitted in the enhanced electric field either by a multi-photon or tunneling process. In the multi-photon regime, that is for small field strengths, an electron absorbs several photons to overcome the potential (work function) of the metal. Tunneling occurs when the potential is bent strongly enough to allow the electron to tunnel through the barrier. Last, the electrons become ponderomotively accelerated by the evenascent fields and gain high kinetic energies.

In particular we are interested in the dependence of the final kinetic electron energies on the surface plasmon resonances, and correspondingly will compare resonant and off-resonant nanoparticles. We also compare simulation and measurement results from the same particles by the cut-off's (highest kinetic electron energy) of the electron spectra. Also the angle and phase dependence of the process will be investigated. The simulation results allow to determine the

spots were the electrons with the highest kinetic energies are emitted.

The thesis is structured into four main parts. The first two chapters deal with the theory behind the involved processes. The first chapter is devoted to the optical excitation of surface plasmons at metal-air interfaces. The second chapter deals with the theory of electron emission including models for multi-photon absorption and tunneling. In chapter three we list the simulation details: The main processes are addressed, which are evaluation of the electromagnetic fields on and away from the particle surface, electron-emission by the electric fields from the metal, and ponderomotive acceleration of the electrons in the total electric field. The last chapter shows the results obtained from simulation and experiment, as well as a detailed comparison.

3. Electromagnetic fields at interfaces

The understanding of hot electron emission from metallic nanoparticles requires a theory to describe the induced fields on the particles (surface plasmons). As we are dealing with sufficiently large particles (dimensions of 100 nanometers) we are safe with a classical description and do not need to stick to quantum theory. The equations are given by famous Clark Maxwell, who unified the existing electromagnetic laws for describing electromagnetic effects, like Faraday's or Gauss's law, to one theory, called classical field theory [21]. The electromagnetic fields are treated as three dimensional, time dependent vector fields, which are determined by their curl and divergence in a medium. To account for the interface between the particle and, e.g., vaccuum we also need boundary conditions between different media.

Applying classical field theory to an interface geometry, we will find a solution with propagating waves at an dielectric/metal interface, so-called surface plasmons, and see that the constraints of excitation are given by the dielectric functions $\epsilon(\omega)$ of the different media.

3.1. Maxwell equations

Maxwell's equations are the backbone of electrodynamics. They combine the electric field $\mathbf{E}(\mathbf{r}, t)$ and the magnetic field $\mathbf{B}(\mathbf{r}, t)$ and read in Gaussian units

and their macroscopic form as [17]

$$\boldsymbol{\nabla} \cdot \mathbf{D}(\mathbf{r}, t) = 4\pi\rho(\mathbf{r}, t), \tag{3.1a}$$

$$\boldsymbol{\nabla} \cdot \mathbf{B}(\mathbf{r}, t) = 0, \tag{3.1b}$$

$$\boldsymbol{\nabla} \times \mathbf{H}(\mathbf{r}, t) = \frac{4\pi}{c}\mathbf{j} + \frac{1}{c}\frac{\partial \mathbf{D}(\mathbf{r}, t)}{\partial t}, \tag{3.1c}$$

$$\boldsymbol{\nabla} \times \mathbf{E}(\mathbf{r}, t) = -\frac{1}{c}\frac{\partial \mathbf{B}(\mathbf{r}, t)}{\partial t}, \tag{3.1d}$$

where, for linear and isotropic media $\mathbf{D} = \epsilon\,\mathbf{E}$ is the dielectric displacement, ρ the free charge density, and $\mathbf{B} = \mu\mathbf{H}$ the magnetic field. Here ϵ is the permittivity, which is assumed to be uniform in each medium. μ is the magnetic permeability. Since we are dealing with light only at optical frequencies we can set $\mu = 1$ throughout [17]. c is the speed of light, and $\mathbf{j}$ refers to the current density.

Equation (3.1a) states that there are electric monopoles. It is called Gauss´s law. Its magnetic analogon equation (3.1b) declares the magnetic field to be free of sources. Equations (3.1c) and (3.1d) are called Ampére's and Faraday's law, and describe that electric/magnetic fields induce a curl magnetic/electric field. If there are no sources present ($\rho = 0$ and $\mathbf{j} = 0$) and assuming solutions with time dependence in the form of[1] $\mathrm{e}^{-i\omega t}$ Maxwell´s equations read in frequency form

$$\boldsymbol{\nabla} \times \mathbf{E}(\mathbf{r}, \omega) = i\frac{\omega}{c}\,\mathbf{B}(\mathbf{r}, \omega) \qquad \boldsymbol{\nabla} \cdot \mathbf{B}(\mathbf{r}, \omega) = 0, \tag{3.2a}$$

$$\boldsymbol{\nabla} \cdot \mathbf{D}(\mathbf{r}, \omega) = 0 \qquad \boldsymbol{\nabla} \times \mathbf{B}(\mathbf{r}, \omega) = -i\frac{\omega}{c}\,\mathbf{D}(\mathbf{r}, \omega). \tag{3.2b}$$

A simple mathematical trick (that is taking the curl on Ampére's law in frequency form) leads to a second order partial differential equation, which is called the Helmholtz wave equation

$$\boldsymbol{\nabla} \times \boldsymbol{\nabla} \times \mathbf{E} = \boldsymbol{\nabla}(\boldsymbol{\nabla} \cdot \mathbf{E}) - (\boldsymbol{\nabla} \cdot \boldsymbol{\nabla})\,\mathbf{E} = -\boldsymbol{\nabla}^2\,\mathbf{E},$$

$$\boldsymbol{\nabla} \times i\frac{\omega}{c}\,\mathbf{B}(\mathbf{r}, \omega) = i\frac{\omega}{c}(-i\frac{\omega}{c}\,\mathbf{D}) = \frac{\omega^2}{c^2}\epsilon\,\mathbf{E} = \epsilon k^2\,\mathbf{E},$$

[1] An arbitrary solution can be made with this ansatz for linear media by Fourier superposition.

with the wavenumber $k = \frac{\omega}{c}$. A similar derivation can be made with Faraday's law, and so we obtain for the electric and magnetic fields

$$(\boldsymbol{\nabla}^2 + \epsilon k^2)\,\mathbf{E}(\mathbf{r},\omega) = 0, \tag{3.3a}$$
$$(\boldsymbol{\nabla}^2 + \epsilon k^2)\,\mathbf{B}(\mathbf{r},\omega) = 0. \tag{3.3b}$$

These are six second order differential equation, which are subject to k and ϵ. By introducing a scalar and vector potential for the electromagnetic fields we are able to reduce them to four uncoupled second order differential equations. This is done in a first step by substituting

$$\mathbf{B} = \boldsymbol{\nabla} \times \mathbf{A}, \tag{3.4a}$$
$$\mathbf{E} = -\boldsymbol{\nabla}\Phi + ik\mathbf{A} \tag{3.4b}$$

into Maxwell's equations (3.2a). There is some arbitrariness in the definition of the potentials: We can choose different gauge transformations for the potentials that leave the fields $\mathbf{E}$ and $\mathbf{B}$ unchanged. This gives us some freedom for manipulations. To uncouple the equations we make use of the so-called Lorenz condition[20]:

$$\boldsymbol{\nabla} \cdot \mathbf{A} - ik\epsilon\Phi = 0. \tag{3.5}$$

With this condition we can express the scalar potential through the divergence of the vector potential and $\boldsymbol{\nabla}\Phi$ through $\boldsymbol{\nabla}(\boldsymbol{\nabla} \cdot \mathbf{A})/ik\epsilon$, and arrive at the Helmholtz wave equation for potentials. They are completely equivalent to Maxwell's equations and read

$$(\boldsymbol{\nabla}^2 + \epsilon k^2)\Phi(\mathbf{r},\omega) = -4\pi\rho(\mathbf{r},\omega), \tag{3.6a}$$
$$(\boldsymbol{\nabla}^2 + \epsilon k^2)\mathbf{A}(\mathbf{r},\omega) = -\frac{4\pi}{c}\mathbf{j}(\mathbf{r},\omega). \tag{3.6b}$$

3.1.1. The quasi-static approximation

If the size of a particle is small compared to the wavelength of the exciting electromagnetic field redartation effects (i.e. dependence of the electromagnetic field on past times) do not play an important role anymore, and we can set the wave number $k = 0$ in equation (3.1.1) . For the Lorenz gauge the vector potential $\mathbf{A}$ thus vanishes. Also the Helmholtz wave equation transforms to

$$\boldsymbol{\nabla}^2\Phi = -4\pi\rho. \tag{3.7}$$

Without external charges this formula reduces to the well known Laplace equation:

$$\boldsymbol{\nabla}^2\Phi = 0. \tag{3.8}$$

One can solve this equation by using a Green's function by searching for a solution of the form

$$\boldsymbol{\nabla}^2 G(\mathbf{r}, \mathbf{r}') = -4\pi\delta(\mathbf{r} - \mathbf{r}'). \tag{3.9}$$

It can be shown, that the following expression is an appropriate choice to fulfill equation (3.9). It is called the Green's function G, which mediates the interaction between two points $\mathbf{r}$ and $\mathbf{r}'$ of the system

$$G(\mathbf{r}, \mathbf{r}') = \frac{1}{\mid \mathbf{r} - \mathbf{r}' \mid}. \tag{3.10}$$

In general, we have to regard the whole volume of the excited system, but if we are dealing with homogeneous media, that is for constant $\epsilon(\omega)$ inside the particles, we can perform a substantial simplification of the problem by converting the volume integration into a surface integration. Then we are safe to write the potential Φ as an integral equation in the ad-hoc form [14]

$$\Phi(\mathbf{r}) = \oint\limits_{\partial\Omega} \sigma(\mathbf{s}')G(\mathbf{r}, \mathbf{s}')da' + \Phi_{ext}. \tag{3.11}$$

It is constructed such, that the *Poisson equation* is fulfilled everywhere, except at the boundaries $\partial\Omega$ of two different media. To involve the boundaries at the different media we have to take care of the boundary conditions for the potentials (given in Appendix A.1):

$$\hat{\mathbf{n}} \cdot (\epsilon_1 \boldsymbol{\nabla}\Phi_1 - \epsilon_2 \boldsymbol{\nabla}\Phi_2) = 0. \tag{3.12}$$

Here ϵ_1 is the permittivity of medium one, ϵ_2 is the permittivity of medium two, and $\hat{\mathbf{n}}$ is a normed vector pointing normal to the interface. So let's evaluate the surface derivative $\hat{\mathbf{n}} \cdot \boldsymbol{\nabla}\Phi$ for the potential of the form (3.11). Here we have to be careful about the singularity in the Green's function at $s = s'$. We perform the limit

$$\lim_{\mathbf{r}\to\mathbf{s}} \hat{\mathbf{n}} \cdot \boldsymbol{\nabla}\Phi(\mathbf{r}) = \lim_{\mathbf{r}\to\mathbf{s}} \left\{ \hat{\mathbf{n}} \cdot \boldsymbol{\nabla} \int\limits_{\partial\Omega} G(\mathbf{r} - \mathbf{s}')\sigma(\mathbf{s}')da' + \hat{\mathbf{n}} \cdot \boldsymbol{\nabla}\Phi_{ext} \right\}.$$

For the case where $\mathbf{s} = \mathbf{s}'$ we carry out the integral

$$\lim_{\mathbf{r}\to\mathbf{s}'} \hat{\mathbf{n}}\cdot\boldsymbol{\nabla}\Phi(\mathbf{r}) = \lim_{\mathbf{r}\to\mathbf{s}'} \hat{\mathbf{n}}\cdot\boldsymbol{\nabla} \int\limits_{\partial\Omega} G(\mathbf{r}-\mathbf{s}')\sigma(\mathbf{s}')da'.$$

Switching to polar coordinates with $\mathbf{r} = (0,0,z)^T$ normal to the surface and $\mathbf{s} = (\cos\phi, \sin\phi, 0)^T$ and for a small circle R where we assume $\sigma(\mathbf{s}') \cong \sigma(\mathbf{s})$ to be a constant we get

$$\lim_{\mathbf{r}\to\mathbf{s}'} \hat{\mathbf{n}}\cdot\boldsymbol{\nabla} \int\limits_{\partial\Omega} G(\mathbf{r}-\mathbf{s}')\sigma(\mathbf{s}')da' = \lim_{z\to\pm 0} 2\pi z \int\limits_0^R \frac{\rho}{(\rho^2+z^2)^{\frac{3}{2}}}\sigma(\mathbf{s})d\rho = \pm 2\pi\sigma(\mathbf{s}).$$

The plus/minus sign depends on whether we approach the surface from medium 1 or medium 2. Filling in the above result we arrive at

$$\lim_{\mathbf{r}\to\mathbf{s}} \hat{\mathbf{n}}\cdot\boldsymbol{\nabla}\Phi(\mathbf{r}) = \lim_{\mathbf{r}\to\mathbf{s}} \left\{ \hat{\mathbf{n}}\cdot\boldsymbol{\nabla} \int\limits_{\partial\Omega} G(\mathbf{r}-\mathbf{s}')\sigma(\mathbf{s}')da' \pm 2\pi\sigma(\mathbf{s}) + \hat{\mathbf{n}}\cdot\boldsymbol{\nabla}\Phi_{ext} \right\}.$$

or in a short-hand notation with $F(\mathbf{s},\mathbf{s}') = \hat{\mathbf{n}}\cdot\boldsymbol{\nabla}G(\mathbf{r}-\mathbf{s}')$ and $\lim\limits_{\mathbf{r}\to\mathbf{s}} \hat{\mathbf{n}}\cdot\boldsymbol{\nabla} = \frac{\partial}{\partial \mathrm{n}}$,

$$\frac{\partial\Phi}{\partial n} = \int\limits_{\partial\Omega} F(\mathbf{s},\mathbf{s}')\sigma(\mathbf{s}')da' \pm 2\pi\sigma(\mathbf{s}) + \frac{\partial\Phi_{ext}}{\partial n} \tag{3.13}$$

An analytic solution for equation (3.13) only exists for a few restricted geometries, e.g. for spherical particles by Gustav Mie [23]. In order to achieve results for arbitrary boundaries $\partial\Omega$ we use a boundary element method [14] and discretize the surface $\partial\Omega$ into small surface elements $\partial\Omega_i$, which changes the integral into a sum:

$$\left(\frac{\partial\Phi}{\partial n}\right)_i = \sum_j F_{ij}\sigma_j \pm 2\pi\sigma_i + \left(\frac{\partial\Phi_{ext}}{\partial n}\right).$$

The above formula can be rewritten as a matrix equation:

$$\frac{\partial\boldsymbol{\Phi}}{\partial n} = \hat{\mathbf{F}}\boldsymbol{\sigma} \pm 2\pi\boldsymbol{\sigma} + \frac{\partial\boldsymbol{\Phi}_{ext}}{\partial n},$$

where $\boldsymbol{\Phi}$, $\boldsymbol{\Phi}_{ext}$ and $\boldsymbol{\sigma}$ are now vectors with the same size as the number of surface elements N and $\hat{\mathbf{F}}$ is a matrix with dimensions $N \times N$. Inserting this into our boundary conditions (3.12) finally leads to an expression for $\boldsymbol{\sigma}$:

$$\boldsymbol{\sigma} = -\left[\hat{\mathbf{\Lambda}} + \hat{\mathbf{F}}\right]^{-1} \frac{\partial \mathbf{\Phi}_{ext}}{\partial n}, \tag{3.14}$$

with

$$\hat{\mathbf{\Lambda}} = 2\pi \frac{\epsilon_2 + \epsilon_1}{\epsilon_2 - \epsilon_1} \mathbb{1}.$$

We note, that $\boldsymbol{\sigma}$ depends (except from the external potential) only on the material parameter $\hat{\mathbf{\Lambda}}$ and on the surface derivative $\hat{\mathbf{F}}$ of the Green function. From the knowledge of $\boldsymbol{\sigma}$ we are now able to solve equation (3.11) and obtain the potential and electric field at every point of our two media.

3.1.2. Solving the full Maxwell equations

When the particle size is no longer sufficiently small compared to the wavelength of the exciting field, the wavenumber $k \neq 0$, and therefore the vector potential does not vanish anymore. Then we have to search for a solution of the full Helmholtz equations (3.1.1). That means, we are looking for the retarded Green's function, which has to obey

$$\left(\boldsymbol{\nabla}^2 + k_j^2\right) G_j(\mathbf{r}, \mathbf{r}') = -4\pi\delta(\mathbf{r} - \mathbf{r}'), \tag{3.15}$$

where $k_j = k\epsilon_j(\omega)$ and $j = 1, 2$ denotes media 1 or 2. A possible solution of equation (3.15) is given by [16, 10]

$$G_j(\mathbf{r}, \mathbf{r}') = \frac{\mathrm{e}^{ik_j|\,\mathbf{r}-\mathbf{r}'\,|}}{|\,\mathbf{r}-\mathbf{r}'\,|}. \tag{3.16}$$

It is now again possible to write the potentials in the ad hoc form as integrals over the particle surfaces by similar considerations as in the quasistatic case

$$\Phi(\mathbf{r}) = \oint_{\partial\Omega_j} \sigma(\mathbf{s}') G(\mathbf{r}, \mathbf{s}')_j da' + \Phi_{ext}(\mathbf{r}), \tag{3.17}$$

$$\mathbf{A}(\mathbf{r}) = \oint_{\partial\Omega_j} \mathbf{h_j}(\mathbf{s}') G(\mathbf{r}, \mathbf{s}')_j da' + \mathbf{A}_{ext}(\mathbf{r}), \tag{3.18}$$

where $\sigma_j(\mathbf{s}')$ and $h_j(\mathbf{s}')$ are the surface charges and currents, respectively, for each medium, and Φ_{ext} and $\mathbf{A}_{ext}$ are the external potentials, e.g. produced by a plane wave or a dipole excitation. The solution (3.18) again satisfies Helmholtz equation (3.1.1) everywhere except at the boundaries $\partial\Omega_j$ and accordingly Maxwell's boundary conditions (see Appendix A.1) lead to the constituting equations for the surface charges and currents for each medium.

3.2. Plasmons

When light interacts with a metal, the electromagnetic response is dictated by the free electrons of the conduction band. Also interband excitations play an important role if the energy of the electric field is large enough to exceed the bandgap of the metal. All phenomena can be described classicaly by the complex dielectric function. If the real part of the dielectric function is negative the free electron gas can be forced by light to have surface charge density oscillations, called surface plasmons, which come together with a strongly enhanced evanescent field at the interface.

We begin with a simple derivation of the dielectric function for metals using the Drude model, and then look for the conditions for the generation of surface plasmons at an interface.

3.2.1. Dielectric function

The optical properties of metals can be characterized by the frequency-dependent dielectric function $\epsilon(\omega)$ which has a real and an imaginary part. As already stressed, the optical behavior is mostly determined by the free motion of the electrons in the conduction band and by interband transitions.

We start with a microscopic description of the interaction between the free electrons and the electric field. The interaction yields a displacement of the electrons $\boldsymbol{\mu} = e\,\mathbf{r}$. Summing up these dipolemomenta for all electrons results in a macroscopic polarization $\mathbf{P} = n\boldsymbol{\mu}$ with n the number of electrons per unit volume.

The macroscopic polarization can be written as

$$\mathbf{P}(\omega) = \chi_e(\omega)\,\mathbf{E}(\omega) \tag{3.19}$$

and

$$\mathbf{D}(\omega) = \epsilon(\omega)\,\mathbf{E}(\omega) = \mathbf{E}(\omega) + 4\pi\chi_e(\omega)\,\mathbf{E}(\omega), \tag{3.20}$$

which leads to the dielectric function in the form of

$$\epsilon(\omega) = 1 + 4\pi\chi_e(\omega). \tag{3.21}$$

The polarization $\mathbf{P}$ and the susceptibility χ_e are obtained by solving the equation of motion of the electrons under the driving force of an external electric field.

Drude-Sommerfeld theory

First, we consider the effect of the driving field for the conduction electrons, which reads according to the Drude-Sommerfeld model (see e.g. [25]), as

$$m_e \frac{\partial^2 \mathbf{r}}{\partial t^2} + m_e \Gamma \frac{\partial \mathbf{r}}{\partial t} = e\,\mathbf{E}_0\,\mathrm{e}^{-i\omega t}, \tag{3.22}$$

with e the charge and m_e the effective mass of a free electron, $\mathbf{E}_0$ the amplitude and ω the frequency of the driving electric field. $\Gamma = \nu_f / l$ denotes a damping term where ν_f is the Fermi velocity and l is the electron mean-free path. We solve equation (3.22) with the ansatz $\mathbf{r}(t) = \mathbf{r}_0\,\mathrm{e}^{-i\omega t}$ and obtain $\mathbf{P}$. Then we get for the susceptibility

$$\chi_e(\omega) = \frac{|\mathbf{P}|}{|\,\mathbf{E}\,|} = -\frac{\omega_p^2}{\omega^2 + i\Gamma\omega} \tag{3.23}$$

with $\omega_p = \sqrt{4\pi n e^2/(m_e)}$ the plasma frequency, and finally

$$\epsilon_{Drude}(\omega) = 1 - \frac{\omega_p^2}{\omega^2 + i\Gamma\omega} \tag{3.24}$$

is the dielectric function for the free electron gas, which is shown in figure 3.1. It reproduces the experimental values e.g. for gold quite accurately above a wavelength $\lambda = 550$ nm. For shorter wavelengths interband transitions come into play and ϵ_{Drude} deviates appreciably from the measured values.

Interband transitions

At short wavelengths or higher photon-energies, transitions from lower bands to the conduction band set in. In a classical picture, we can make a similar ansatz as before to describe the response of the lower lying band:

$$m \frac{\partial^2 \mathbf{r}}{\partial t^2} + m\gamma \frac{\partial \mathbf{r}}{\partial t} + \alpha\,\mathbf{r} = e\,\mathbf{E}_0\,\mathrm{e}^{-i\omega t}, \tag{3.25}$$

where m is the effective mass of the bound electrons, γ is again a damping term and α is the spring constant of the binding potential. We find in the same way as before

$$\epsilon_{interband}(\omega) = 1 + \frac{\tilde{\omega}_p^2}{(\omega_0^2 - \omega^2) - i\gamma\omega}, \tag{3.26}$$

with $\tilde{\omega}_p = \sqrt{\tilde{n}e^2/(m)}$ and $\tilde{n}$ the density of bound electrons. Furthermore, we introduce a new constant $\omega_0 = \sqrt{\alpha/m}$. Figure 3.1 shows a plot of $\epsilon_{Drude+interband}$ where the peak in the imaginary part at around 450 nm is attributed to the interband transition. Now the model is in good agreement with the experimental values, espescially when we only look at wavelengths larger than 450 nm.

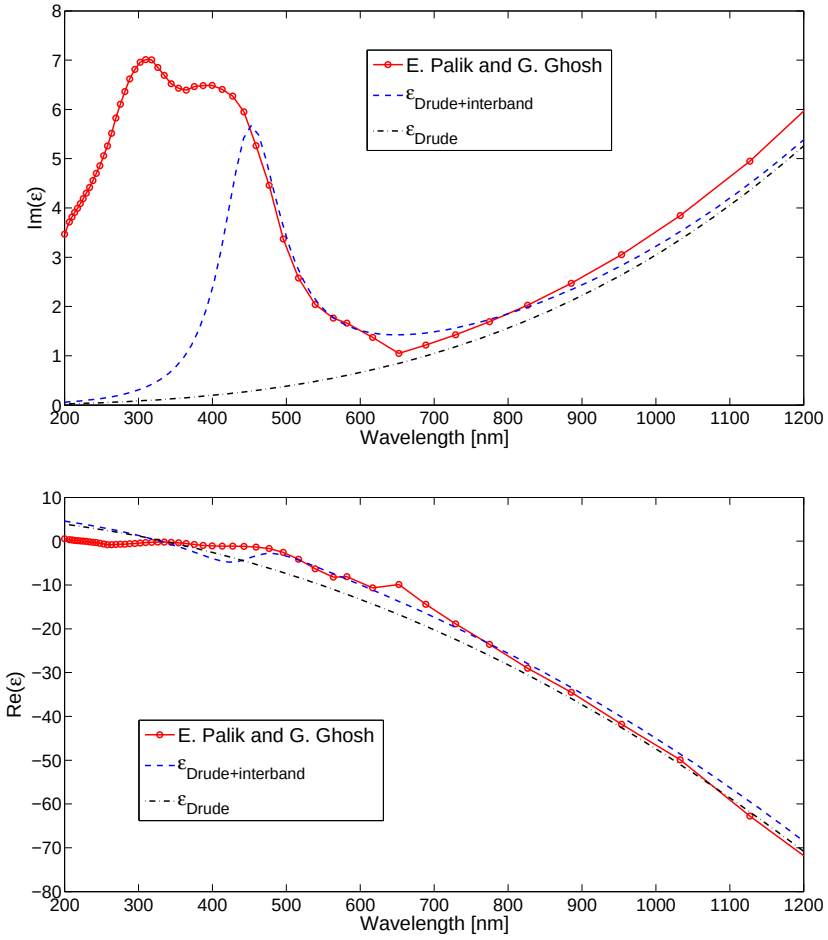

Figure 3.1.: Imaginary and real part of the dielectric function of gold: The experimental values taken from [26] agree for optical wavelengths with the Drude model if interband transitions are taken into account and a constant offset $\epsilon_\infty = 6$ is introduced, which accounts for all higher-energy band transitions. Below $\lambda = 450$nm the model is still inappropriate.

3.2.2. Surface plasmons at interfaces

Following [25], we will now derive the dispersion relation for surface plasmons, that are collective surface charge oscillations at an interface. We consider a plane interface in the xy-plane between the media shown in figure 3.2. One medium is characterized by a real dielectric function $\epsilon_1(\omega)$, e.g. vacuum or air, and the other by a complex dielectric function $\epsilon_2(\omega)$, e.g. a metal. We are looking for solutions of the wave equation (3.3a)

$$\left(\boldsymbol{\nabla}^2 + \epsilon(\omega)\frac{\omega^2}{c^2}\right)\mathbf{E}(\mathbf{r},\omega) = 0, \tag{3.27}$$

together with boundary conditions for the interface. In general the electric field can be split into two components, one parallel and one perpendicular to the plane of incidence (defined by the k-vector of the plane wave and the surface normal $\hat{\mathbf{n}}$ of the interface). The perpendicular component is called s-polarized (from german 'senkrecht' - perpendicular) or TE-mode (transversal-electric), and the parallel is named p-polarized or TM-mode (transversal-magnetic). There is no homogeneous solution existing for the case of s-polarization, so we deal with p-polarized electric fields E_j only ,where $j = 1, 2$ is the index to the media

$$\mathbf{E}_j = \begin{pmatrix} E_{j,x} \\ 0 \\ E_{j,z} \end{pmatrix} \mathrm{e}^{i(k_x x + k_{j,z} z - \omega t)} \tag{3.28}$$

Since the wave vector component parallel to the interface is conserved, the following relation for the wave vectors holds:

$$k_x^2 + k_{j,z}^2 = \epsilon_j k^2, \tag{3.29}$$

with $k = 2\pi/\lambda$. From equation (3.2b) we find

$$k_x E_{j,x} + k_{j,z} E_{j,z} = 0. \tag{3.30}$$

Inserting into the equation of p-polarized plane waves (3.28) leads to

$$\mathbf{E}_j = E_{j,x} \begin{pmatrix} 1 \\ 0 \\ -k_x/k_{j,z} \end{pmatrix} \mathrm{e}^{i(k_x x + k_{j,z} z - \omega t)}. \tag{3.31}$$

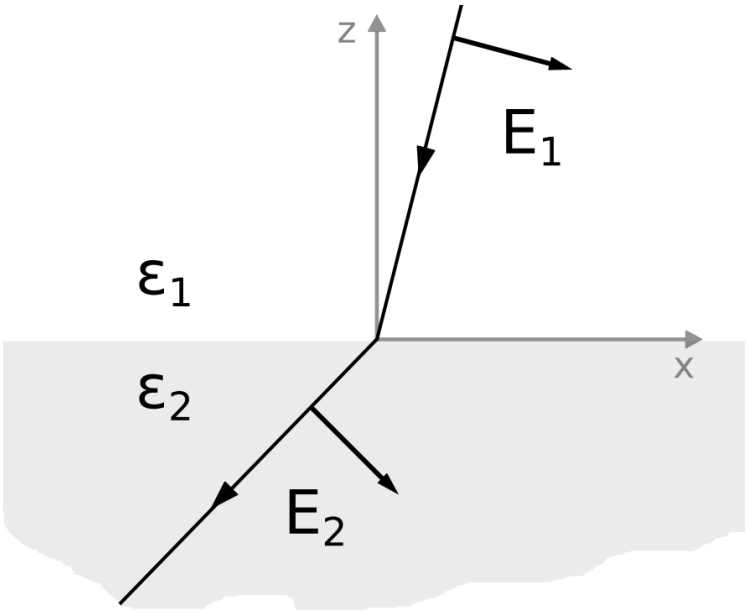

Figure 3.2.: Electric field at a plane interface with two different media. We are dealing only with p-polarized light.

What is left to do is to impose the boundary conditions at the interface (see Appendix A.1), which read for our problem

$$\begin{aligned} E_{1,x} - E_{2,x} &= 0, \\ \epsilon_1 E_{1,z} - \epsilon_2 E_{2,z} &= 0. \end{aligned} \tag{3.32}$$

So we get four equations for four unknowns, namely equations (3.30) and (3.32). We require that the determinant of the set of equations vanishes. This is the case for either $k_x = 0$, where we clearly do not get excitations traveling along the interface, or

$$\epsilon_1 k_{2,z} - \epsilon_2 k_{1,z} = 0. \tag{3.33}$$

The above solution leads together with the condition that the wave vector component parallel to the surface is conserved, which is described in equation (3.29), to a relation between the wave vector component along the interface direction and the angular frequency ω:

$$k_x^2 = \frac{\epsilon_1 \epsilon_2}{\epsilon_1 + \epsilon_2} k^2 = \frac{\epsilon_1 \epsilon_2}{\epsilon_1 + \epsilon_2} \frac{\omega^2}{c^2}, \tag{3.34}$$

$$k_{j,z}^2 = \frac{\epsilon_j^2}{\epsilon_1 + \epsilon_2} k^2. \tag{3.35}$$

For a wave traveling along the surface we require a real k_x. This can be achieved if the sum and product of the real parts of the dielectric functions are either positive or negative. Next, in order to reach a "bound" solution we want $k_{j,z}$ to be purely imaginary, which means that the field is trapped at the surface and can not travel into the media. In order to fulfill both of these conditions, we need for the dielectric functions the properties

$$\epsilon_1(\omega) \cdot \epsilon_2(\omega) < 0, \tag{3.36}$$

$$\epsilon_1(\omega) + \epsilon_2(\omega) < 0. \tag{3.37}$$

So, one dielectric function must be positive and the other must be negative. Also the absolute value of the negative dielectric function has to be greater than the otherone. Metals, especially noble metals such as gold or silver, are a good choice for exciting surface plasmons. This can be seen in figure 3.1 for gold, where the real part of the dielectric function is negative and much larger than e.g the dielectric constant of air, which is around one.

In order to excite a plasmon we have to fulfill momentum and energy conservation. So let us look at the dispersion relation we just derived to see how it can be done.

Excitation of surface plasmons

We take $\epsilon_1 = 1$ (e.g. air), and for ϵ_2 the Drude function for gold, but neglect the imaginary part, that is we do not consider dissipative effects. A plot of the dispersion relation for the surface wave, according to equation (3.35) is given in figure 3.3. We see that in order to fulfill momentum and energy conservation, we have to tilt the light line. This can be done by slowing down light with a dielectric medium, for example with the so called *Kretschmann configuration* or the *Otto configuration* [25].

Particle plasmons

Until now we have talked about plasmons which are confined to a surface with infinite extension. If we consider nanosized particles, we have a closed surface, where the system is in general no longer translational invariant and the electron density oscillations are bound to the surface structure. Furthermore, the wave number is no longer conserved. In a simplified picture, the free electrons act like a oscillator and at resonance they have a phase shift of 90 degrees with

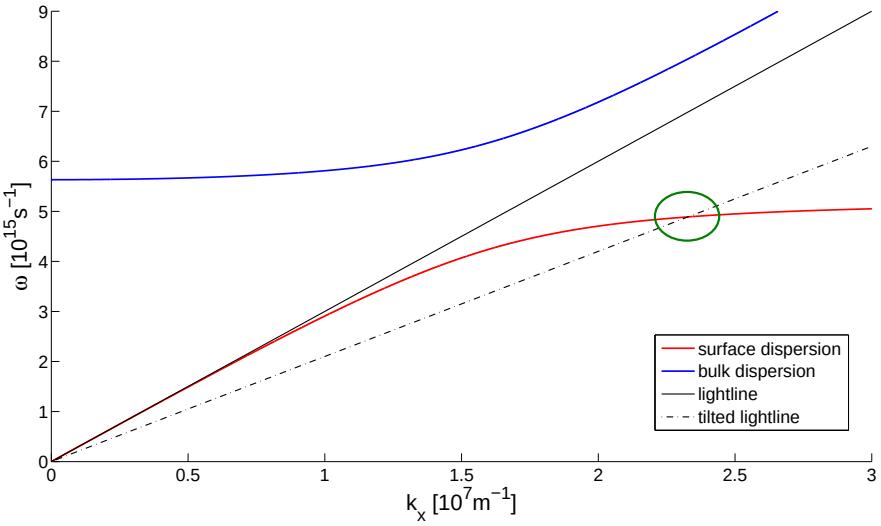

Figure 3.3.: Dispersion relation for the Drude model. The red line shows the light dispersion for exciting a plasmon confined to the surface. Dashed, light line tilted by a factor $\omega = ck_x/n$. The point where the tilted light line matches the surface dispersion relation is shown by the green ellipse. The blue line accounts for the excitation of a bulk plasmon, where the wavevector in z-direction is a real quantity.

respect to the exciting field. If the resonance is red-shifted with respect to the exciting field the phase-shift is 180 degree, whereas blue-shifted particles have a phase-shift of zero degrees.

4. Nonlinear Photoionization

Ionization of electrons in sufficiently strong laser fields can either take place by photon absorption or by tunneling through the barrier.

The theoretical description of this processes is best understood for atoms. Approaches for a metal surface are difficult, but the description for atoms matches, at least qualitatively, the one for surfaces. So we will restrict ourself to the basic processes studied by atoms. A first, and also commonly used approach was formulated by Keldysh [18]. In his work a so called adiabacity parameter γ accounts quantitatively for the transition between multiphoton and tunneling electron emission

$$\gamma = \sqrt{\frac{\Phi}{2U_p}}, \tag{4.1}$$

where

$$U_p = \frac{e^2 E_0^2}{4 m_e \omega^2},$$

E_0 is the peak electric field strength of the exciting field, Φ is the binding energy of the electron and ω is the circular frequency of the exciting field. In the case of a metal this is the work function ϕ, which is the work done by an electron to escape from the metal (e.g. for gold $\phi = 5.1$ eV). In the limit $\gamma \gg 1$ (low electric field strength compared to $\frac{\omega\sqrt{4m_e\Phi}}{e}$) a multiphoton process takes place and in the limit $\gamma \ll 1$ (high electric field strength with respect to $\frac{\omega\sqrt{4m_e\Phi}}{e}$) tunneling occurs. According to Einstein's work, for which he received the Nobel-price [8], the photon-energy has to fulfill $\omega > E_i$ in order to emit an electron from a metal by photon absorption. In the visible regime we typically have 1 eV$< \omega <$ 2 eV and therefore $\omega < E_i$. However, if more than one photon excites the electron the ionization condition can be satisfied with $k\omega > E_i$, where k is the number of photons needed to overcome the binding energy. In figure 4.1 we see a three-photon process (k =3) schematically. As the interaction in the multiphoton regime is sufficiently small, we will use perturbation theory in section 4.1 to describe the multiphoton process.

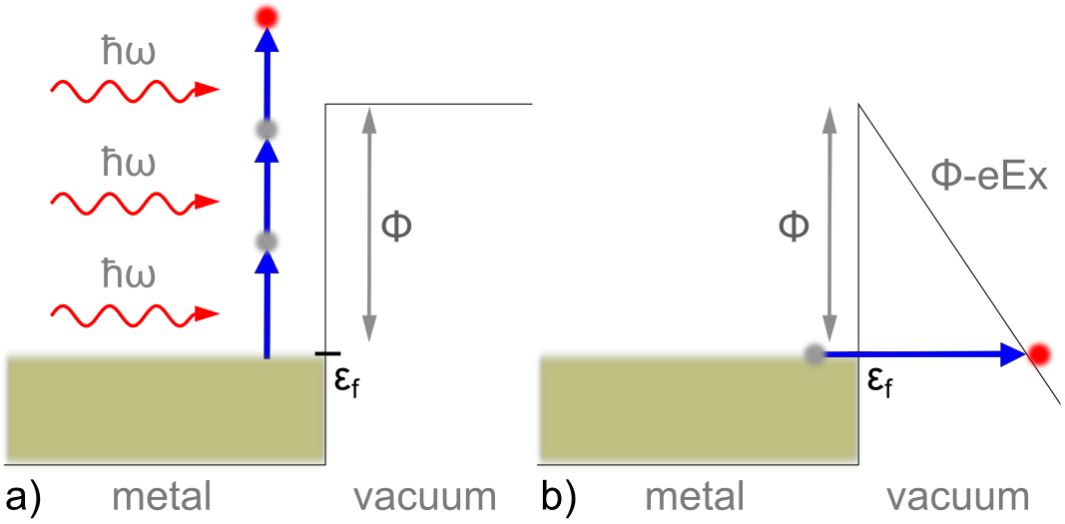

Figure 4.1.: a) Multi-photon process. Each absorbed photon raises the energy of an electron by $\hbar\omega$ to intermediate states until the electron escapes from the potential. b) Tunneling process: the barrier is bent strongly by the electric field, which allows an electron to tunnel through the barrier.

In the tunneling regime (depicted in figure 4.1b) a perturbation technique is no longer possible because the interaction between the electric field and the system is too strong and, thus we solve our system with a different technique assuming a short range potential. This was done e.g. by Keldysh, Krainow and Delone and others [6, 18, 5]. We will derive the Wentzel-Kramer-Brillouin approximation, which gives the correct exponential factor for tunneling, and summarize the Keldysh approach. Also the Yudin-Ivanov formula, a non-adiabatic expression for the emission probability describing both regimes, will be discussed.

4.1. Multiphoton process

In this section we will derive the perturbative solution of an ionization process. The derivation follows [3]. We want to solve the time-dependent Schrödinger equation

$$i\hbar\frac{\partial\Psi(\mathbf{r},t)}{\partial t} = H\Psi(\mathbf{r},t). \tag{4.2}$$

The Hamiltonian of our system can be written as an unperturbed Hamiltonian H_0 and a part interacting with the electric field $H_1 = qV = -eV$, where $V = -\mathbf{r} \cdot \mathbf{E}$,

$$H = H_0 + \boldsymbol{\mu} \cdot \mathbf{E}(t). \tag{4.3}$$

Here we introduced $\boldsymbol{\mu} = e\,\mathbf{r}$ the interaction energy with the exciting field. We assume the electric field to be a plane wave switched on suddenly at $t = 0$, that is

$$E(t) = E_0\, \mathrm{e}^{-i\omega t} + c.c. \tag{4.4}$$

The solution of the Schrödinger equation without a perturbation can be written in the form

$$\Psi_n(\mathbf{r}, t) = u_n(\mathbf{r})\, \mathrm{e}^{-i\omega_n t}\,. \tag{4.5}$$

Inserting into the time-dependent Schrödinger, we find that $\omega_n = E_n/\hbar$, if $u_n(\mathbf{r})$ satisfies

$$H_0 u_n(\mathbf{r}) = E_n u_n(\mathbf{r}), \tag{4.6}$$

where E_n are the eigenvalues of the unperturbed system. The solution of (4.2) can be written as a linear combination of energy eigenstates of H_0, which form a complete set,

$$\Psi(\mathbf{r}, t) = \sum_l a_l(t) u_l(\mathbf{r})\, \mathrm{e}^{-i\omega_l t}\,. \tag{4.7}$$

Plugging equation (4.7) into equation (4.2), making use of the orthonormality condition $\int u_m^*(\mathbf{r}) u_l(\mathbf{r}) d^3r = \delta_{ml}$, integrating over all space and multiplying with $u_m^*(\mathbf{r})$ from the left, we obtain

$$i\hbar \frac{da_m}{dt} = \sum_l a_l(t) V_{ml}\, \mathrm{e}^{-i\omega_{lm} t}, \tag{4.8}$$

with $\omega_{lm} = \omega_l - \omega_m$ (here we get a first glimpse of the condition for a transition), and

$$V_{ml} = \int u_m^*(\mathbf{r}) V u_l(\mathbf{r}) d^3r \tag{4.9}$$

is the matrix element for transitions from level l to level m. Equation (4.8) can not be solved exactly, so we will use perturbation technique to gain some insight. We impose a continuous parameter λ that goes from zero to one, where $\lambda = 1$ corresponds to the whole interaction and replace V_{ml} by λV_{ml}. Next we write $a_m(t)$ in a power series of λ

$$a_m(t) = a_m^0(t) + \lambda a_m^1(t) + \lambda^2 a_m^2(t) + \cdots\,. \tag{4.10}$$

Inserting (4.10) into (4.8), with our new interaction λV_{ml}, and sorting in powers of λ we get

$$i\frac{da_m^N}{dt} = \sum_l a_l^{N-1}(t) V_{ml}\, \mathrm{e}^{-i\omega_{lm}t}, \tag{4.11}$$

where $N = 1, 2, 3....$ This is an iterative set of equations. So we can calculate the N-th order of the power series (4.10) by using the (N-1)-th order, and for N = 0 we already have the result of H_0.

One photon absorption

Having derived (4.11), we are ready to describe the process of one photon absorption by setting N=1 and assuming our unperturbed system to be in state g, which means

$$a_g^0(t) = 1, \quad a_l^0 = 0 \text{ for } l \neq g \tag{4.12}$$

We can write the interaction (4.4) by use of equation (4.9) as

$$V_{mg} = -\mu_{mg}\big(E\, \mathrm{e}^{-i\omega t} + E^*\, \mathrm{e}^{i\omega t}\big), \tag{4.13}$$

where $\mu_{mg} = e\int \mu_m^*(\mathbf{r}\cdot\hat{\mathbf{n}})\mu_g d^3r$ and $\hat{\mathbf{n}}$ is the vector in $\mathbf{E}$ direction. Now we have on the right side of equation (4.11) only the term $a_g^0(t)$, and we evaluate by integration $a_m^1(t)$:

$$\begin{aligned} a_m^1(t) &= -(i\hbar)^{-1}\mu_{mg}\int_0^t \big[E\, \mathrm{e}^{i(\omega_{mg}-\omega)t} + E^*\, \mathrm{e}^{i(\omega_{mg}+\omega)t}\big] \\ &= \frac{\mu_{mg}E}{\hbar(\omega_{mg}-\omega)}\big[\mathrm{e}^{i(\omega_{mg}-\omega)t} - 1\big] + \frac{\mu_{mg}E^*}{\hbar(\omega_{mg}+\omega)}\big[\mathrm{e}^{i(\omega_{mg}+\omega)t} - 1\big]. \end{aligned} \tag{4.14}$$

In the expression above, the first term can get resonant for one photon absorption, that is if $\omega_{mg} = \omega$, whereas the second term describes a one photon emission process. Since we are interested in an absorption process we ignore the second term. This simplification is known as the rotating wave approximation. The probability to be in the state m is then given by

$$p_m^1(t) = |a_m^1(t)| = \frac{|\mu_{mg}E|^2}{\hbar^2}\left|\frac{\mathrm{e}^{i(\omega_{mg}-\omega)t}-1}{\omega_{mg}-\omega}\right|^2 = \frac{|\mu_{mg}E|^2}{\hbar^2} f(t). \tag{4.15}$$

It can be shown that for large t

$$\lim_{t\to\infty} f(t) = 2\pi t\delta(\omega_{mg} - \omega), \tag{4.16}$$

where $\delta(x - x_0)$ is the well known Dirac delta-function. So we write for the probability of being in the state m

$$p_m^1(t) = \frac{|\mu_{mg}E|^2}{\hbar^2} t 2\pi\delta(\omega_{mg} - \omega). \tag{4.17}$$

Since the probability is increasing with time we define a probability per unit time or transition rate determined by

$$P_m^1 = \frac{d}{dt}p_m^1 = \frac{|\mu_{mg}E|^2}{\hbar^2} 2\pi\delta(\omega_{mg} - \omega). \tag{4.18}$$

To account for a continuous final state m, we finally multiply the transition rate with the number of states dm and integrate over the final states. This gives

$$\begin{aligned} P_m^1 &= \int_{-\infty}^{\infty} \frac{dm}{dE_m} dE_m \frac{|\mu_{mg}E|^2}{\hbar^2} 2\pi\delta(\omega_{mg} - \omega) \\ &= \frac{|\mu_{mg}E|^2}{\hbar^2} 2\pi\rho_m\big|_{\omega_{mg}=\omega}, \end{aligned} \tag{4.19}$$

where $\rho_m = dm/dE_m$ is the energy density of the unperturbed final states. It is convenient to describe the absorption in terms of an absorption cross section $\sigma_{mg}^1(\omega)$, leading to

$$P_m^1 = \sigma_{mg}^1(\omega) I. \tag{4.20}$$

Here $I = 2n\epsilon_0 c|E|^2$ and

$$\sigma_{mg}^1(\omega) = \frac{\pi}{n\epsilon_0 c} \frac{|\mu_{mg}|^2}{\hbar^2} \rho_m\big|_{\omega_{mg}=\omega}. \tag{4.21}$$

Multi photon ionization

In a similar manner, we can evaluate two photon ionization, which is solving equation (4.11) for $N = 1$ and $N = 2$. Since the idea of the derivation is the

same as for one photon ionization, we will restrict ourself to the result for the ionization probability (for the derivation see Appendix B.2 or [3] or [6]):

$$P_n^2 = \sigma_{ng}^2(\omega) I^2, \tag{4.22}$$

$$\sigma_{ng}^2(\omega) = \frac{\pi}{2n^2\epsilon_0^2 c^2} \left| \sum_m \frac{\mu_{nm}\mu_{mg}}{\hbar^2(\omega_{mg} - \omega)} \right|^2 \rho_n \big|_{\omega_{ng}=2\omega}. \tag{4.23}$$

So, if there are no resonances with level m than this is a nice result. But because of the possible singularity at $\omega_{mg} = \omega$, for intermediate resonance levels we would have to stick to another description, which can be found e.g. in [6] . The result (4.23) can be easily generalized to higher-order processes. We see from (4.20) and (4.23) that the photon ionization probability is proportional to the intensity and the intensity squared, respectively. This holds also in general:

$$P_i^k \propto \sigma_{ig}^k(\omega) I^k. \tag{4.24}$$

Finally we note that the perturbative approach deals with a time-averaged ionization probability. The intensity of the electric field is to be taken as an absolute value, where the oscillations of the plane wave excitation have canceled out.

4.1.1. Above-threshold ionization

In the multiphoton limit, according to perturbation theory, the number of photons needed to free an electron is $k = \langle \Phi/\omega \rangle$, where Φ is the work function, ω is the frequency of the exciting field and the brackets stand for the integer value. For intermediate values of $\gamma \approx 1$ the electron can gain more photons than needed to overcome the barrier, which is called above threshold ionization. Then the electron absorbs an energy of $\epsilon = \hbar\omega(k+s)$ where the portion of $\hbar\omega k$ is used to overcome the ionization potential and $\hbar\omega s$ is left as kinetic energy. Therefore these above threshold electrons start with a velocity unequal to zero.

This effect can be seen at field strengths beginning from about 10 V/nm [31]. From sharp metal tips there have been reported up to six additional absorbed photons [28].

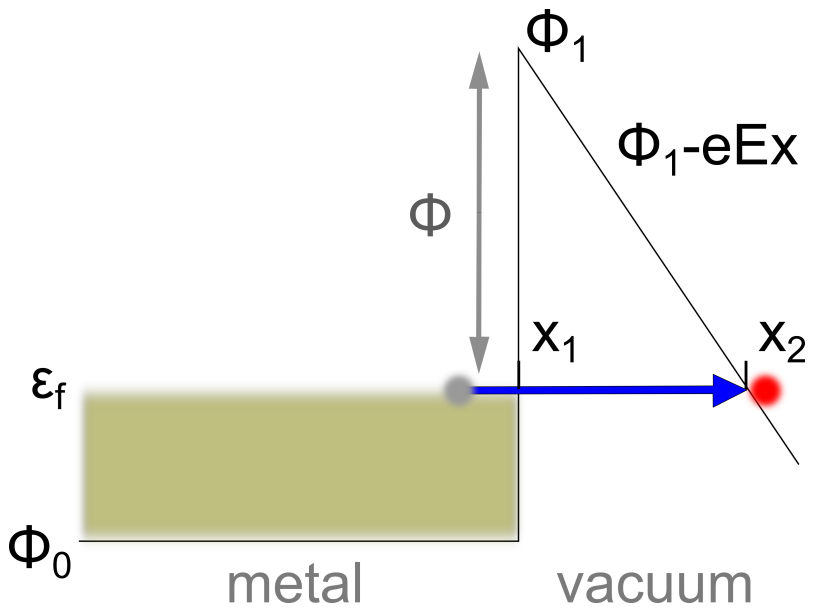

Figure 4.2.: Potential and turning points for the Wentzel-Kramer-Brillouin method. Here, ϵ_f denotes the Fermi-energy.

4.2. Tunneling

Tunneling occurs only for intense laser fields where the Keldysh parameter $\gamma \ll 1$. Then, the potential where the electron is captured is bent strong enough (see figure 4.1) to let tunneling occur. With the WKB-approximation, we will derive the exponential factor of the emission probability for the one-dimensional stationary case. Then the Keldysh approach, where a time-varying field is assumed, is discussed, and extensions of the Keldysh approach are summarized. Last, we will represent a non-adiabatic emission rate, the Yudin-Ivanov formula, which accounts for multiphoton processes, tunneling and the regime in between.

4.2.1. The WKB-approximation

We derive the tunneling rate $T(\epsilon)$ for a static electric field using the Wentzel-Kramer-Brillouin approximation [30]. Starting with the one-dimensional stationary Schrödinger equation

$$\left(-\frac{\hbar}{2m_e}\frac{\partial^2}{\partial x^2} + V(x)\right)\Psi(x) = \epsilon\Psi(x), \tag{4.25}$$

we evaluate the transmission probability for an arbitrary barrier with two turning points (see Appendix B.17) as

$$T(\epsilon) = \exp\left(-\frac{2}{\hbar}\int_{x_1}^{x_2}\sqrt{2m_e(V(x)-\epsilon)}dx\right). \tag{4.26}$$

For our problem (depicted in figure 4.2) the potential reads

$$V(x) = \begin{cases}\Phi_0 & x < 0,\\ \Phi_1 - eEx & x \geq 0,\end{cases} \tag{4.27}$$

where e and m_e are the electron charge and mass. The turning points are at $x_1 = 0$ and $x_2 = \frac{\Phi_1-\epsilon_f}{eE}$. By inserting the potential (4.27) and the turning points, the integral in (4.26) takes the form

$$\int_0^{x_2}\sqrt{2m_e(\Phi_1 - eEx - \epsilon_f)}dx = \frac{2\sqrt{2m_e}(\Phi_1-\epsilon_f)^{3/2}}{3eE}.$$

So the transmission probability finally reads

$$T(\epsilon_f) = \exp\left(-\frac{4\sqrt{2m_e}(\Phi_1-\epsilon_f)^{3/2}}{3\hbar eE}\right). \tag{4.28}$$

4.3. Keldysh-theory

There are several ways to derive the main result of the Keldysh approach that is the transition probability of a time-varying field. E.g., one can use a s-matrix approach [18, 5] or the Landau-Dykhne adiabatic approximation [6]. Here we will give a short review of the first one and follow the derivation of [5].

The transition amplitude from an initial state i to a final free state f is given by the matrix element between the initial unperturbed wave function Ψ_i and the exact final wave function in the continuum Ψ_f:

$$a_{if} = -i\int_0^t \langle\Psi_i|\, V(r,t')\,|\Psi_f\rangle\, dt', \tag{4.29}$$

where $V(r,t)$ is the interaction potential of the electron with the electromagnetic field. The Keldysh derivation replaces the exact final wave function by the wave function of an electron in an electromagnetic field $\Psi_f^{(V)}$, which reads

$$\Psi_f^{(V)}(\mathbf{r},t) = (2\pi)^{-3/2} \exp\left[i\,\mathbf{r}(\mathbf{p}+\mathbf{A}(t)/c) - \frac{i}{2}\int_0^t (\mathbf{p}+\mathbf{A}(t')/c)^2 dt' \right]. \quad (4.30)$$

Here $\mathbf{A}$ is the vector potential of the electromagnetic field. It is related to the field strength by $\mathbf{E}(t) = -(1/c)d\mathbf{A}/dt$. As an interaction we use the dipole approximation of an electron in an electromagnetic field:

$$V(\mathbf{r},t) = -e\,\mathbf{r}\cdot\mathbf{E}(t). \quad (4.31)$$

By inserting equation (4.30) in equation (4.29) and deriving the integral by the saddle-point method [18], one obtains an expression for the ionization rate, which is in the case of a linearly polarized electromagnetic field

$$T \propto \exp\left[-(2E_i/\omega)f(\gamma)\right], \quad (4.32)$$

$$f(\gamma) = \left(1+\frac{1}{2\gamma^2}\right)\sinh^{-1}\gamma - \frac{1}{2\gamma}\sqrt{1+\gamma^2}, \quad (4.33)$$

where γ is the Keldysh-parameter and E_i is the energy of a single bound state.

Limiting cases

In the limit $\gamma^2 \ll 1$ $f(\gamma)$ reduces to $f(\gamma) = \frac{2}{3}\gamma$ and we find for the transmission probability

$$T = \exp\left[-\frac{4\sqrt{2}|E_i|^{3/2}}{3E}\right], \quad (4.34)$$

which is within exponential accuracy the transmission probability of an electron in a static field (see subsection 4.2.1).

In the multiphoton limit, when $\gamma \gg 1$ we find for $f(\gamma) = \ln(2\gamma/e^{1/2})$ and T reduces to

$$T = \left(\frac{e^{1/2}E}{2(2|E_i|)^{1/2}\omega}\right)^{2|E_i|/\omega}. \quad (4.35)$$

This result coincides with the perturbative derived multiphoton expressions of the $|E_i|/\omega^{th}$ order in subsection 4.1, where $|E_i|/\omega = k$ is the number of photons needed to excite an electron from the bound state into the continuum.

4.3.1. Extensions of the Keldysh approach

Extensions of the Keldysh approach appeared shortly after its publication [24]. The so-called PPT-theory [27] generalizes the transmission probability to three dimensions and is applicable for hydrogen atoms with arbitrary initial ground states of a projection quantum number m in direction of the electric field, a principal quantum number n and an orbital angular momentum l.

A generalization of the PPT-theory is given by Ammosov, Delone and Krainov [1] for linearly polarized light, who used instead of the principal quantum number n an effective principle quantum number n^*, which accounts for complex atoms or atomic ions.

Other approaches, especially for metal surfaces, where reflections at the surface are taken into account or the exact Schrödinger equation is solved numerically with a Cranck-Nicholson procedure can be found in [31].

Yudin-Ivanov formula

In contrast to the above mentioned models, which all lead to results averaged over one oscillation cycle, the Yudin-Ivanov formula [33] computes the instantaneous tunneling probability in a linearly polarized electric field (see also figure 4.3). The derivation is also based on the Landau-Dykhne adiabatic and the strong field approximation. The transition probability reads

$$T(t) \propto \exp\left(-\frac{E^2 f_p(t)^2}{\omega} f(\gamma(t), \phi(t))\right), \tag{4.36}$$

where E is the electric field strength, $f_p(t)$ is the pulse envelope and $f(\gamma(t), \phi(t))$ is a function dependent on the instantaneous Keldysh parameter γ and phase ϕ of the electric field. The assumption for this formula is that the laser envelope changes between two cycles are small.

The instantaneous probability is strongly depending on the value of the Keldysh parameter (see figure 4.3). In the multiphoton limit the probability is almost constant during the period of the field, whereas in the tunneling regime we observe a strong dependence on the electric field: When the electric field is peaked also the ionization rate has its maximum.

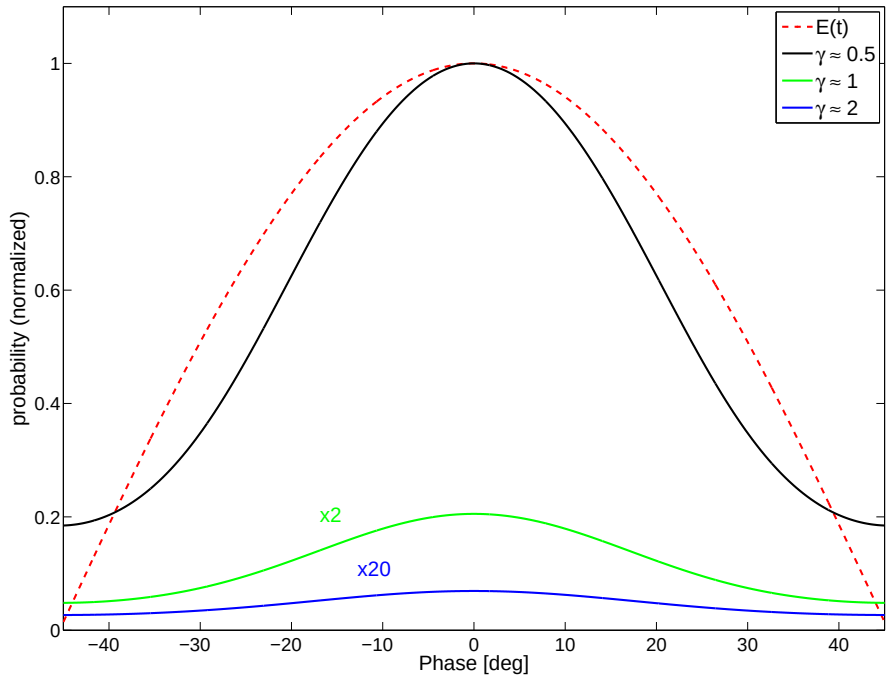

Figure 4.3.: Instantenous tunneling ionization rates given by the Yudin-Ivanov formula as a function of the phase of the exciting laser. Red curve shows the electric field strength, black line is the normalized tunneling ionization rate for $\gamma \ll 1$, green the probability for $\gamma \approx 1$ and blue line is the probability in the multiphoton regime $\gamma \gg 1$.

5. Simulation

5.1. Simple man's model

The simulation of electron trajectories is carried out with the so called simple-man's model [4, 7], where first electrons are photoemitted from the surface and then oscillate and get accelerated by the total electric field (exciting plus induced) of the nanoparticle, which is computed with a boundary element method. In our simulation we place the electrons after the photoemission, either through a multiphoton or a tunneling process, right above the centroids of the boundary elements. After a sufficiently long time (about 50 fs), when the electrons have moved sufficiently far away from the particle and do not feel the acceleration of the induced electric field anymore, the simulation ends and we obtain their final kinetic energies ϵ_{kin}. This procedure runs for different phases ϕ of the plane wave excitation with the restriction that only at positive values of the total electric field electron emission takes place. Then the accelerating force is pointing away from the surface. So the total electric field reads

$$\mathbf{E}(\mathbf{r}, t, \phi) = Re\big[\mathrm{e}^{-i(\omega+\phi)t}\big(\mathbf{E}_{exc}(\mathbf{r}, \omega) + \mathbf{E}_{ind}(\mathbf{r}, \omega)\big)\big], \tag{5.1}$$

where ω is the frequency of the plane wave excitation, $\mathbf{E}_{exc}(\mathbf{r}, \omega)$ and $\mathbf{E}_{ind}(\mathbf{r}, \omega)$ are the exciting and induced fields in the frequency domain at the point $\mathbf{r}$, respectively, which we evaluate with a boundary element method.

5.1.1. Boundary element method

The discretization as well as the computation of the spectra and the electric fields is done with the MNPBEM-Toolbox [15]. For the optical excitation $\mathbf{E}_{exc}(\mathbf{r}, \omega)$ we use a plane wave excitation with a wavelength of $\lambda = 800$nm.

First of all, one has to discretize the particle surface into small boundary elements as shown for a rectangular and a bowtie-geometrie particle in figure 5.1. The surface charges are placed at the centroids of each element. Now

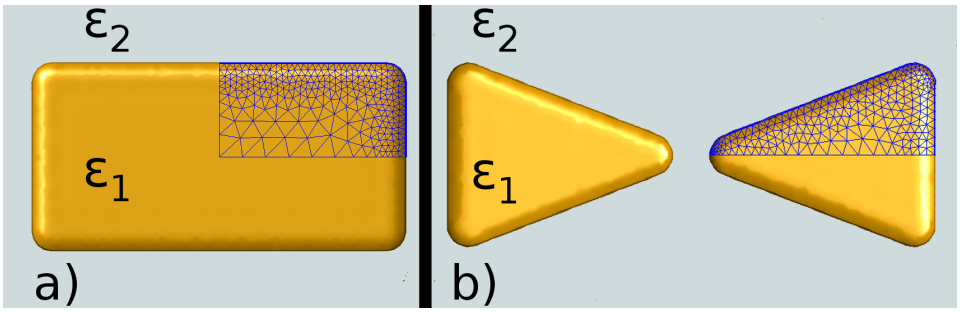

Figure 5.1.: a) Rectangular particle b) bowtie geometrie. The blue lines show the discretization of the particles used in the simulation. ϵ_1 is the dielectric function of gold, values used are from experiment. $\epsilon_2 = 1.3$ is the effective dielectric function of the surrounding and accounts for a mixture of glass and ITO used in experiments.

we are able to evaluate equation (3.28) for different geometries and obtain the surface charges at each boundary element, which allows us to compute the electric fields everywhere else. In a similar manner we solve the full Maxwell equations and obtain surface charges and currents for the evaluation of the electric (and magnetic) field $\mathbf{E}_{ind}(\mathbf{r}, \omega)$. Then we are, in order to achieve the resonance wavelength of a particle, in position to evaluate the particle spectra (extinction, scattering and absorption cross section). These are computed with [17]

$$C_{sca} = n_b \oint_{\partial\Omega} Re\big[\hat{\mathbf{n}}(\mathbf{E} \times \mathbf{B}^*)\big] da, \tag{5.2}$$

$$C_{ext} = -\frac{1}{n_b} \oint_{\partial\Omega} Re\big[\hat{\mathbf{n}}(\mathbf{E} \times \mathbf{B}^*_{inc} + \mathbf{E}^*_{inc} \times \mathbf{B})\big] da, \tag{5.3}$$

$$C_{abs} = C_{ext} - C_{sca}, \tag{5.4}$$

where n_b is the refractive index of the embedding medium, $\mathbf{E}_{inc}$, $\mathbf{B}_{inc}$ are the exciting electromagnetic fields and $\mathbf{E}$, $\mathbf{B}$ are the scattered electromagnetic fields. The integration is taken over a sphere at infinity around the particle, but it is also possible to define a surface (e.g from a detector).

Armed with the fields we are ready to evaluate the electron trajectories.

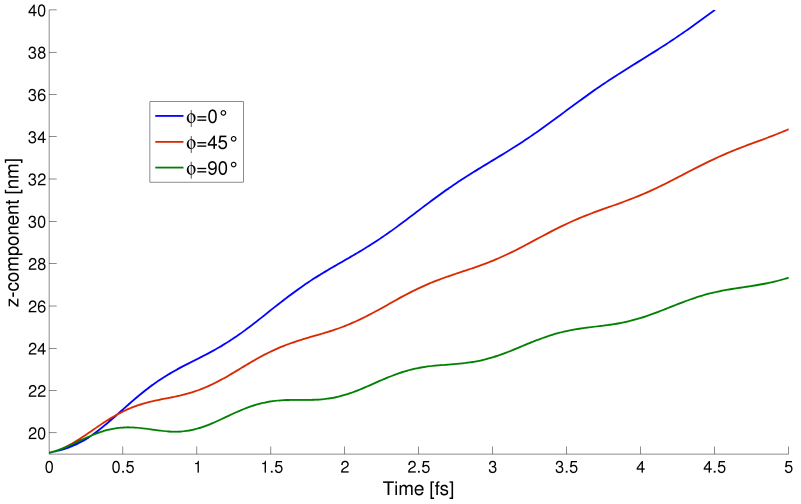

Figure 5.2.: Z-component of an electron from one boundary element moving in the electric field of a nanoparticle for different phases of the exciting laser.

5.1.2. Electron trajectories

In order to compute the final electron energies ϵ_{kin} we place right above each boundary element an electron and then accelerate it with $\mathbf{E}(\mathbf{r}, t, \phi)$:

$$m_e \ddot{\mathbf{r}} = -e\,\mathbf{E}(\mathbf{r}, t, \phi), \tag{5.5}$$

where m_e is the electron mass and e is the electron charge. After a sufficiently long time, when the induced evanescent field $E_{ind}(\mathbf{r}, \omega)$ is not affecting the particle anymore we obtain the final kinetic energy $\epsilon_{kin} = \frac{m_e \mathbf{v}^2}{2}$ of the electron.

The numerical scheme for the solution of the semiclassical Newton's equations of motion is a simple velocity Verlet algorithm [29] with an error of $O(\Delta t^2)$, where we stepwise calculate the position, velocity and acceleration of the particle:

$$\begin{aligned} \mathbf{r}(t+\Delta t) &= \mathbf{r}(t) + \mathbf{v}(t)\Delta t + \frac{E(\mathbf{r}, t, \phi)\Delta t^2}{2}, \\ \mathbf{v}(t+\Delta t) &= \mathbf{v}(t) + \frac{\big(E(\mathbf{r}, t, \phi) + E(\mathbf{r}, t+\Delta t, \phi)\big)\Delta t}{2}. \end{aligned} \tag{5.6}$$

As was derived in section 4.1 in the multiphoton limit, that is for Keldysh parameters $\gamma \gg 1$, the energy of the electron is raised by the electric field

always by a portion of $\hbar\omega$, which is for an excitation with a wavelength of $\lambda = 800$ nm about 1.5 eV. Therefore, with a work function of gold $\Phi = 5.1$ eV and a four-photon process, which is needed to overcome the barrier of gold, a kinetic energy of approximately 1 eV is left. To account for this initial energy we assume the electron to have in the multiphoton limit a starting energy of 1 eV with a velocity pointing in the direction of the surface normal. In contrast, in the tunneling regime with Keldysh parameters $\gamma \ll 1$ the electron has no initial energy. In figure 5.2 we show the z-component of an electron trajectory obtained from the described algorithm for different phases of the exciting laser. In the first periods of the exciting field the electron is accelerated in z-direction, whereas at later times it moves with almost constant velocity.

For different values of the plane wave excitation $\mathbf{E}(\mathbf{r}, \omega)$ we found, that the final energies of the electrons scale linearly with the intensity $|\mathbf{E}_{exc}(\mathbf{r}, \omega)|^2$ as shown for a large number of boundary elements in figure 5.3. This relation is formulated for the boundary element k as

$$\epsilon^k_{kin}(\phi) = \lambda^k |\mathbf{E}_{exc}(\phi)|^2, \tag{5.7}$$

where

$$\lambda^k = \frac{\epsilon^k_{kin,0}(\phi)}{|\mathbf{E}_{exc,0}(\phi)|^2},$$

and $\epsilon^k_{kin,0}(\phi)$ denotes the final kinetic energy of the electron starting from boundary element k of the simulation and $\mathbf{E}_{exc,0}(\phi)$ stands for the external electric field strength of the simulation. The simulation time for one field strength is quiet long, but in a manageable framework to be executed. For a more realistic scenario of the exciting electric field than a plane wave excitation, for example a Gaussian laser pulse, one would have to sum up over a large number of different field strengths, and therefore simulation results, which is too time consuming. But provided with this scaling law we are in position to do so, by just simulating one exciting field strength and then using the scaling law to average over the laser pulse. We note that this procedure is limited to a sufficiently long pulse duration, where the acceleration of the electron can be approximated by the acceleration of a plane wave excitation, or in other words $\tau_p \gg \tau_e$, where τ_p is the laser pulse duration and τ_e is the electron escape time, i.e. the time needed for the electron to escape from the induced evenascent field $\mathbf{E}_{ind}$.

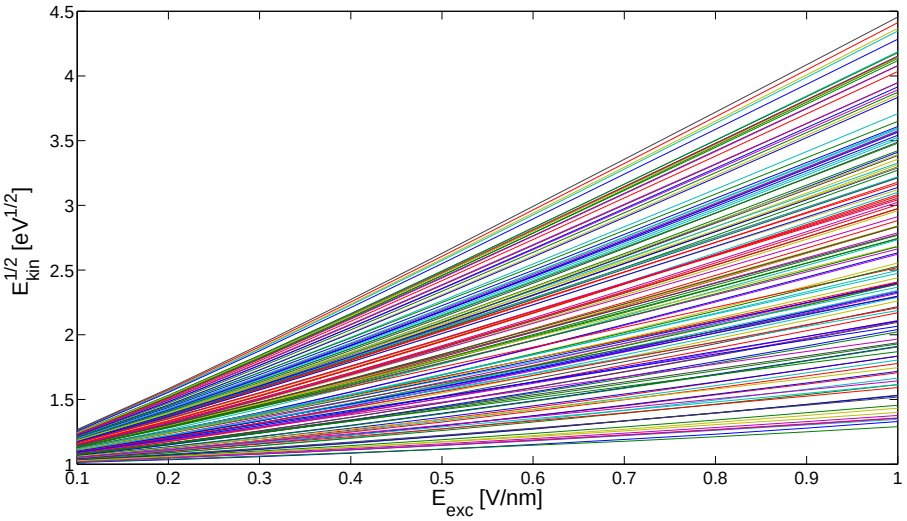

Figure 5.3.: Final kinetic energies as a function of exciting intensity for a large number of boundary elements. Here the linear relation of equation (5.7) is shown for values of E_{exc} from $0.1 - 1\mathrm{V/nm}$ in steps of $0.1\mathrm{V/nm}$ at a phase of $\phi = 0$.

5.1.3. Emission probability

As already derived in chapter 4 the electron emission probability is depending on the Keldysh parameter γ. For values of $\gamma \gg 1$ electron emission takes place in the multiphoton regime, whereas for $\gamma \ll 1$ the barrier is bent strong enough and tunneling occurs.

In the multiphoton limit the emission probability is almost constant during one laser cycle and scales with

$$P(\mathbf{E}(\mathbf{r}, t = 0, \phi)) \propto |\,\mathbf{E}(\mathbf{r}, t = 0, \phi)|^{2n}, \tag{5.8}$$

where n is the number of photons needed to overcome the work function of the material. With a wavelength of the electric field of $\lambda = 800$ nm every absorbed photon raises the electron energy by 1.5 eV. So we assume a four photon process in the simulation, which is sufficient to overcome the work function $\Phi = 5.1$ eV of gold.

As γ decreases to the tunneling limit, the emission probability gets phase dependent and has an exponential dependence on the field strength, as can be

seen from equation (4.28):

$$T(\mathbf{E}(\mathbf{r}, t=0, \phi)) = A(\mathbf{E}(\mathbf{r}, t=0, \phi)) \exp\left(-\frac{4\sqrt{2m_e}(\Phi)^{3/2}}{3\hbar e|\,\mathbf{E}(\mathbf{r}, t=0, \phi)|}\right). \tag{5.9}$$

Usually the pre-exponential factor in (5.9) is obtained from the Fowler-Nordheim approach [9] and reads

$$A(\mathbf{E}(\mathbf{r}, t=0, \phi)) = C|\,\mathbf{E}(\mathbf{r}, t=0, \phi)|^2, \tag{5.10}$$

where C is a constant depending on the mass of the electron in the dielectric and the work function.

To account for both effects, the effective multiphoton emission probability and the phase dependent tunneling regime, we use a non-adiabatic ionization probability, the Yudin-Ivanov formula [33], which interpolates between the two regimes and produces an instantenous, phase dependent ionization rate.

Nonetheless the Yudin-Ivanov formula produces a good estimate for the ionization rate at metal surfaces at both $\gamma \ll 1$ and $\gamma \gg 1$ until today there is no simple method available to describe the complex regime in between.

5.1.4. Electron spectra

Prepared with the scaling law (5.7) and the probabilities for emission we are in the position to obtain a distribution function of final kinetic electron-energies by summing over different phases and the Gaussian laser pulse and weighting with the respective emission probabilities $P(\mathbf{E})$. To do so, we sample over the Gaussian pulse

$$\mathbf{E}_{exc}(t, \phi) = \mathbf{E}_{exc,0}(\phi)\, \mathrm{e}^{-t^2/2}, \tag{5.11}$$

and determine the initial electric field strength which gives the specified final kinetic energy $\epsilon_{kin}(t)$ (derived with (5.7)). In other words, we use

$$f(\epsilon) = \sum_k a^k \int_0^{2\pi} d\phi \int_{-\infty}^{\infty} dt \delta(\epsilon - \epsilon_{kin}(t)) P(\mathbf{E}^k(t, \phi)), \tag{5.12}$$

where a^k denotes the area of the k-th boundary element. We sum over the boundary elements for the phases $(0, 2\pi)$ where the initial electric field is pointing away from the surface and integrate over the Gaussian pulse. The Dirac-delta function δ picks the $\epsilon = \epsilon_{kin}(t)$ out and $P(\mathbf{E}^k)$ weighs them with the respective emission probability.

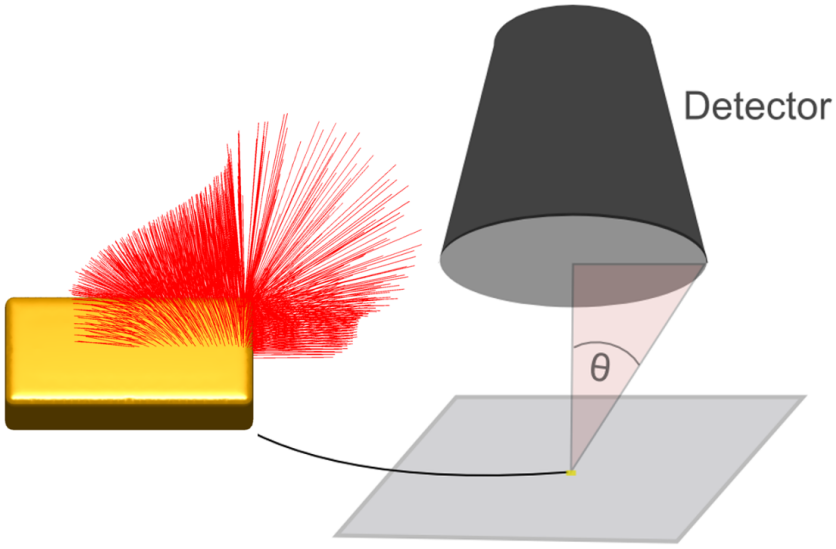

Figure 5.4.: Acceptance cone to account for experimental setup. Usually a detector with a given acceptance cone placed above the nanoparticles measures the electrons. So the electron spectra depend on the polar angle Θ. As the dimensions of the particle compared to the length of the electron flight to the detector is very small a point-like particle can be assumed and we don't need to take into account the spatial distribution of the different emitted electrons.

5.1.5. Acceptance cone

To account for experimental setup, where usually only a certain solid angle of emitted electrons is measured, we introduce an acceptance cone, which only picks out the emitted electrons within a certain emission angle. A typical situation is shown in figure 5.4.

In the simulation first the electron trajectories from all boundary elements are computed and then the angle in z-direction from the starting point to the end point is evaluated by

$$\Theta_s = \arccos\left(\frac{\hat{\mathbf{n}}_z \cdot (pos_{end} - pos_{start})}{|pos_{end} - pos_{start}|}\right), \tag{5.13}$$

where pos_{start} and pos_{end} denote the starting respectively the end point of the trajectory and $\hat{\mathbf{n}}_z$ is the normal vector in z-direction. Then the trajectories with $\Theta < \Theta_s$ are omitted from the final distribution and only the ones which are inside the acceptance cone are taken into account.

6. Results

In this chapter we present and discuss the simulation results. As this master thesis was accompanied with an experiment done by the group of Peter Dombi, we will sometimes also show the experimental data and see how good they agree with the simulations. For the gold nanoparticles we used a dielectric function extracted from experiment [26]. As a simplification we used in the simulation an effective dielectric constant $\epsilon = 1.3$ for the embedding medium, which is motivated by an average value of air and the ITO covered glass substrate. Because of the effective embedding medium, the dimensions of the simulated particles were slightly adapted to match the resonances of the lithographically fabricated particles from the experiment.

In the first section we show the extinction spectra of the simulated particles and obtain their resonance wavelengths. Then we look for the motion of the electrons emitted from the nanoparticles, which gives us insight in the time and spatial dependence of the process. Afterwards we look for the quantitative electron spectra and see how they depend on acceptance cone and resonance wavelength. We will also take a look at the distribution for different emission spots. Finally we see how the computed spectra agree with measured electron distributions.

6.1. Spectra

In the extinction spectra of the different particles, which were computed with the MNPBEM-Toolbox as described in subsection 5.1.1, we can clearly see a pronounced peak, where the dipole-excitation of the surface plasmon is located. So we are in resonance, if we match this peak with the wavelength of the exciting laser pulse by adapting the dimensions of the particle. Then the induced field is phase-shifted by 90 degree, whereas in the off-resonant case, we get a phase-shift of zero degree or 180 degree, depending on whether the particles are red-shifted or blue-shifted. For shorter particles we see that the

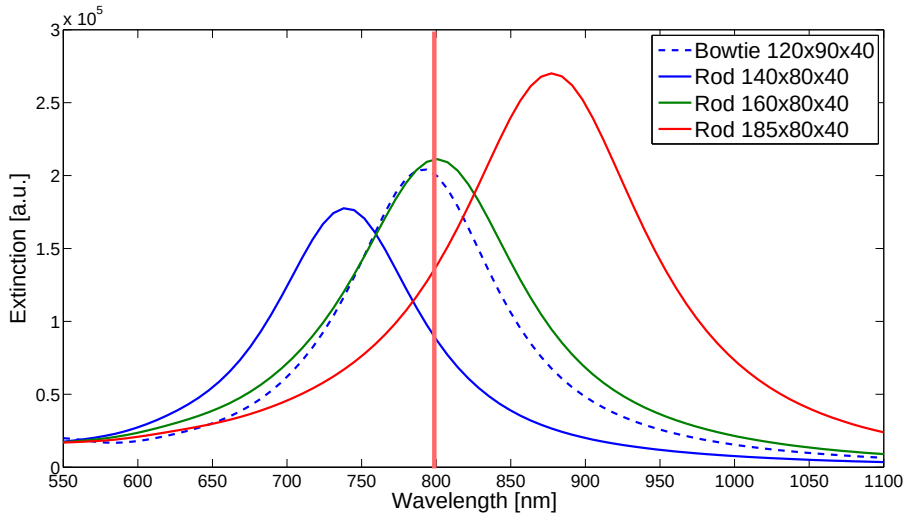

Figure 6.1.: Simulated particle spectra for different particle sizes of rod (continuous lines) and bowtie geometrie (dashed). The resonances of the spectra were matched with the experimental ones. The wavelength of the excitation was chosen to be $\lambda = 800$ nm (same as experiment).

resonance of the particle shifts into the region of smaller wavelength, whereas for longer particles the peak is shifted to the region of larger wavelengths.

6.2. Field enhancement

The field enhancement of the plasmonic nanoparticle plays an important role in the emission of hot electrons because of two points. First the evanescent field accelerates the electrons, and second the emission probability depends on the strength of the field. Therefore the parameters which lead to stronger or weaker electromagnetic fields determine the electron distribution.

As commonly known, plasmonic structures lead to a field enhancement of the exciting field, which is sensitive to the geometry and the resonance of the nanostructure. At the resonance we get the highest field enhancement, whereas for off-resonant particles the enhancement is less strong. A comparison between different geometries is given in figure 6.2. As we see, the field enhancement depends strongly on the chosen geometry. Also the curvature of the particles plays an important role: smaller radii lead to a stronger enhancement at the

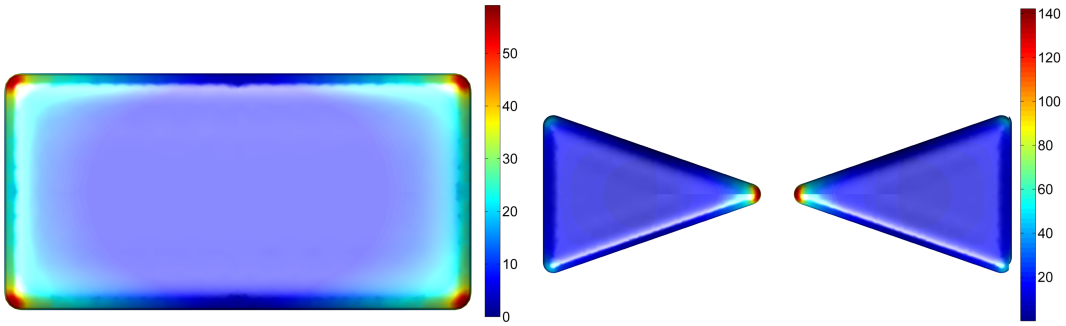

Figure 6.2.: Field enhancement $|\mathbf{E}_{ind}|/|\mathbf{E}_{exc}|$ of rectangular and bowtie particle.

corners and edges of rods and triangles, whereas larger radii give a wider hot-spot at the corners and edges, but lower fields.

6.3. Electron trajectories

The electron trajectories are obtained from the simple-man's model described in chapter 5. The electrons are initially placed right above the boundary elements, and then get accelerated by the electric field. After a sufficiently long time, that is when the electrons are not subject to the induced field anymore and just oscillate accelerated by the exciting field around a certain mean value, the trajectories end. As we see in figure 6.3 the electrons get accelerated most at the first two to four periods of the electric field. As the field strength of the induced field $\mathbf{E}_{ind}$ is depending on the geometry of the particle surface, we get stronger fields at some areas, so called hot-spots. These are mainly the edges and corners and for the bowtie-geometrie the so called feed gap region. Therefore, at these hot-spots the electrons gain more kinetic energy from the electric field.

6.3.1. Phase dependence

The electrons are emitted by multiphoton and tunneling processes at different phases of the laser pulse, and then get accelerated by the total electric field. As is shown in figure 6.4 the electrons at small values of laser pulse phase $\phi \approx 0$ acquire the highest final kinetic energies, but do not contribute much to the total distribution, whereas the emitted electrons at $\phi \approx \pi/2$, that is where the

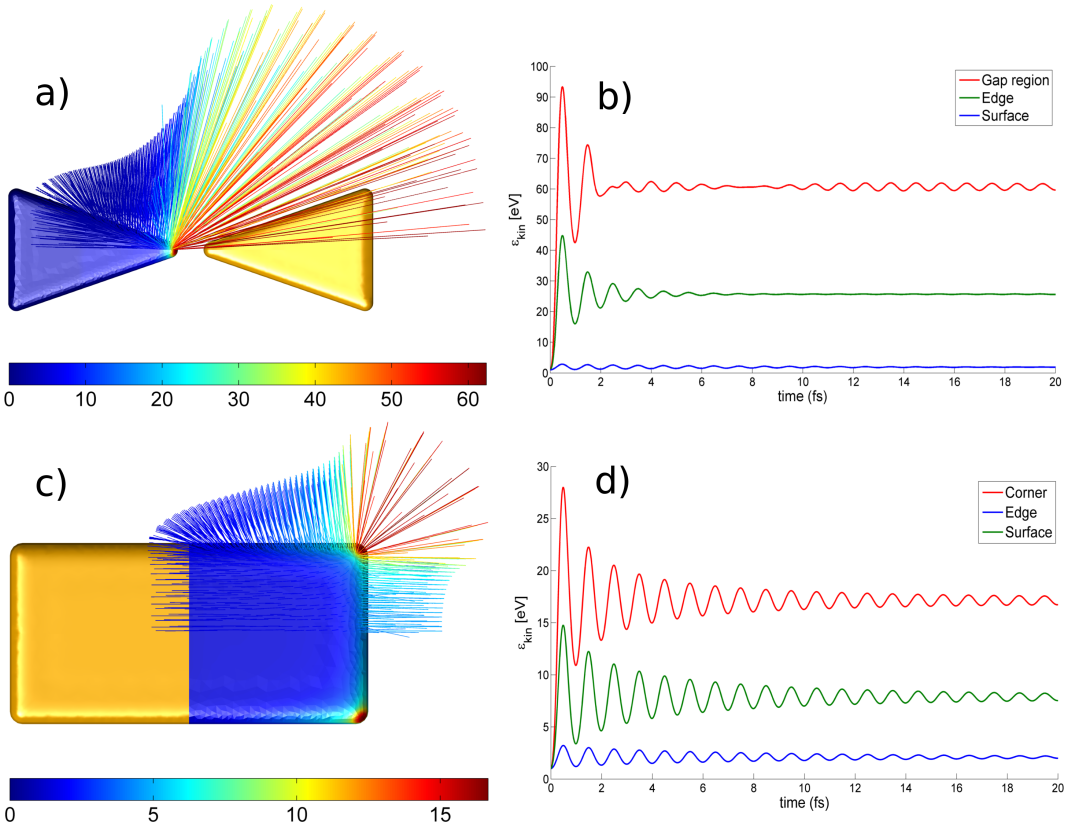

Figure 6.3.: Simulation results of electron trajectories for $E_{exc} = 0.5$ V/nm corresponding to a laser intensity of 35 GW/cm^2. a) Trajectories of a bowtie particle with dimensions 120x90x40 nm^3. The colors of the trajectories show the final kinetic energy ϵ_{kin} of the electrons. At the hot spots ϵ_{kin} up to 60 eV are simulated. b) Kinetic energy of electrons over time for a bowtie particle at different emission spots. Electrons are accelerated mainly by the induced field at the first couple of periods and then oscillate around a certain value. After the first acceleration the kinetic energy can be as large as 90 eV. c) Same as a), but for a rectangular particle with dimensions 160x80x40 nm^3. Here the highest $\epsilon_{kin} \approx 17$ eV at the corner is lower than for bowties. d) same as b) but for rectangular particle.

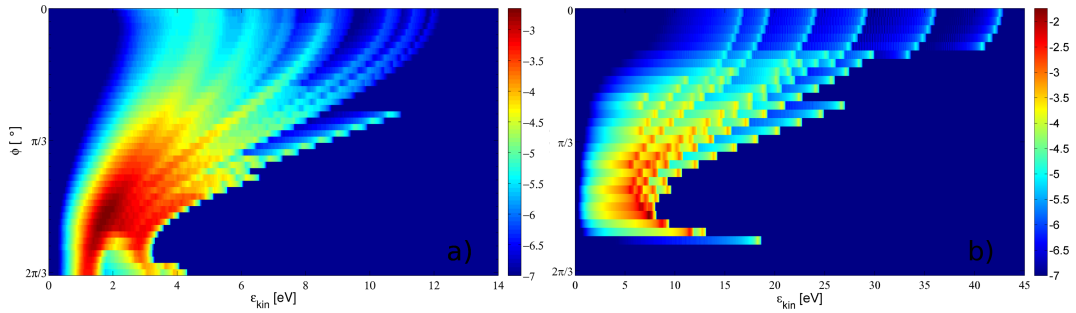

Figure 6.4.: a) Electron distribution (logarithmic) for a rod-particle dimensions 160x80x40 nm^3 dependent on final kinetic electron energies ϵ_{kin} and phase of photoemission ϕ of an exciting laser pulse with intensity 46 GW/cm^2 and $\lambda =$ 800 nm. b) Same as a) but for bowtie geometrie with dimensions 130x90x40 nm^3 and an laser intensity of 35 GW/cm^2.

induced field is strongest, do contribute most to the electron distribution and have values of ϵ_{kin} around $2-3$ eV. In fact, the different amounts of electrons at different phases is due to the photo-emission probability, which is also peaked at the highest intensities (see figure 4.3) where the induced field is strongest.

6.3.2. Angle dependence

As we see in figure 6.5 the electron emission is angle dependent: The highest kinetic electron energies are observed at angles larger than 30 degree, whereas at small angles we observe only very slow electrons. A comparison between rectangular and bowtie particles yields a similar behavior, although the highest final kinetic electron energies are for bowtie antennas by a factor of about four higher than for rectangular particles at the same excitation intensity.

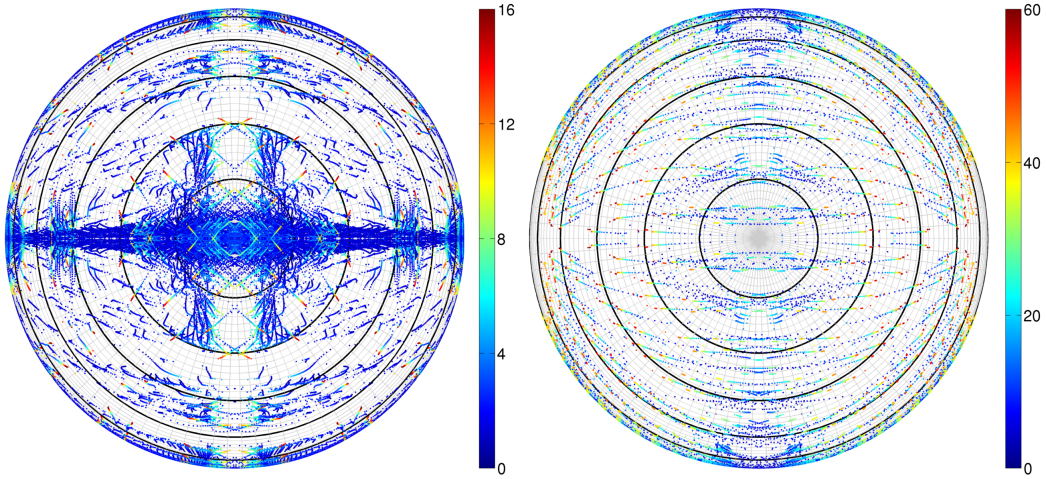

Figure 6.5.: Angle dependence of hot electrons. Colored points correspond to the final kinetic energy of electrons of (left) rectangular particle and (right) bowtie particle. Simulations were carried out at a laser field strength of 0.5 V/nm. Interval between black circles is 15 degree (zero degree in the middle).

6.4. Electron distribution

To obtain the electron distribution we weight the final kinetic electron energies derived from the electron trajectories with the emission probability and the area at the surface elements and average over the Gaussian laser pulse as described in chapter 5.

6.4.1. Surface distribution

As already mentioned the field-enhancement of the nanoparticles strongly depends on the chosen surface spot. For instance rectangular particles have a strong field-enhancement at the corners and edges (see figure 6.2). This is also seen in the electron emission distribution (figure 6.6), where the corners and edges contribute most to the final distribution, although their surface area is small compared to the planar faces. Also the yield from the hottest electrons comes from the edges and especially from the corners (see also figure 6.3).

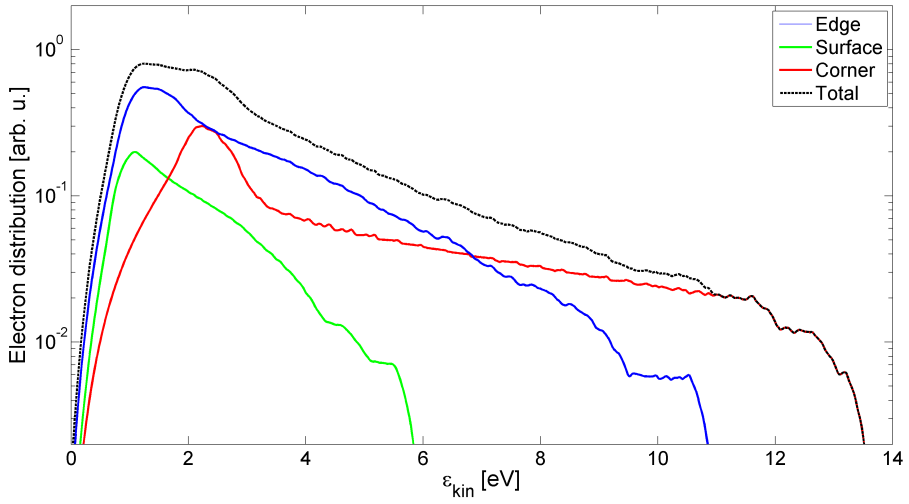

Figure 6.6.: Electron distribution of a resonant rectangular particle with dimensions 160x80x40 nm^3 for different surface areas at an intensity of 35 GW/cm^2 and a wavelength of 800 nm. Surface denotes the planar parts of the particle.

6.4.2. Angle dependence

The electron-distribution of metallic nanoparticles is strongly angle-dependent (see figure 6.7). For instance, the highest kinetic electron energies at an intensity of 33 GW/cm^2 for rectangular particles are around 15 eV and for bowtie structures around 45 eV at an angle of about 30 degree, whereas at an angle of five degrees there are only very slow electrons with kinetic energies of 2-3 eV.

How can this be understood? The induced evenascent field $\mathbf{E}_{ind}$ is pointing mainly in the direction normal to the surface. As the acceleration of the electrons is governed by $\mathbf{E}_{ind}$, whereas the exciting field $\mathbf{E}_{exc}$ does not play an important role, the electron trajectories are also pointing in the direction parallel to the surface normal of each boundary element. So, as we are dealing with curvatures at the hot spots (edges and corners) we get especially at these spots of fast electrons and high electron emission probability a strong angle dependence (see also figure 6.3).

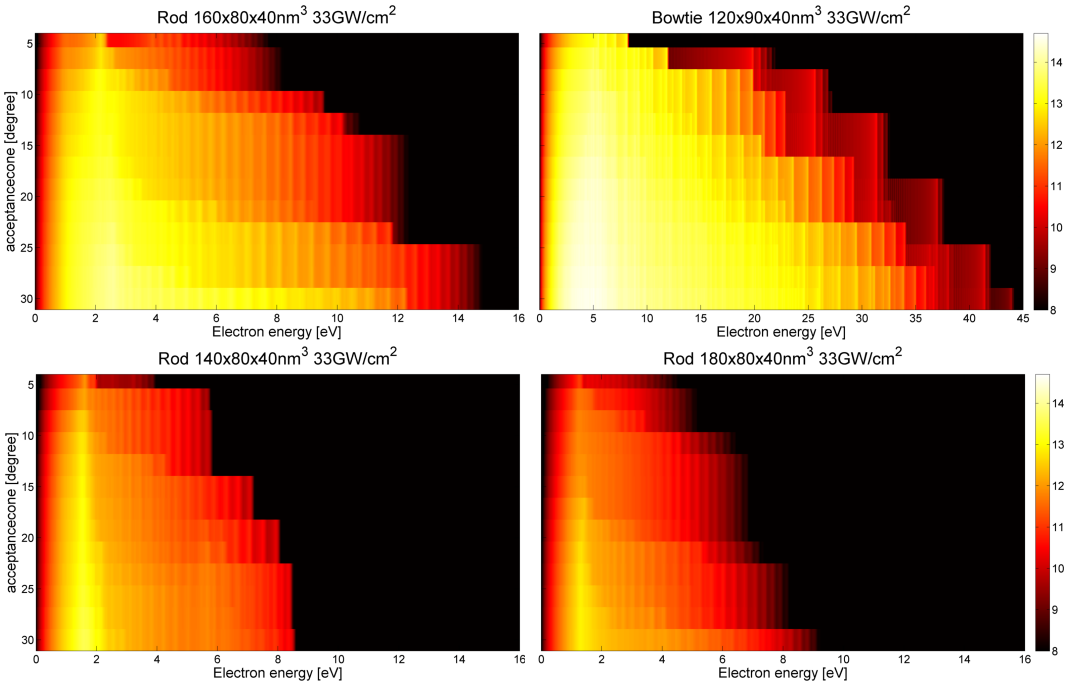

Figure 6.7.: Angle dependence of electron distribution (logarithmic color plot) for resonant (top left) rod, off-resonant rods (bottom) and (top right) bowtie particle at an intensity of 33 GW/cm^2.

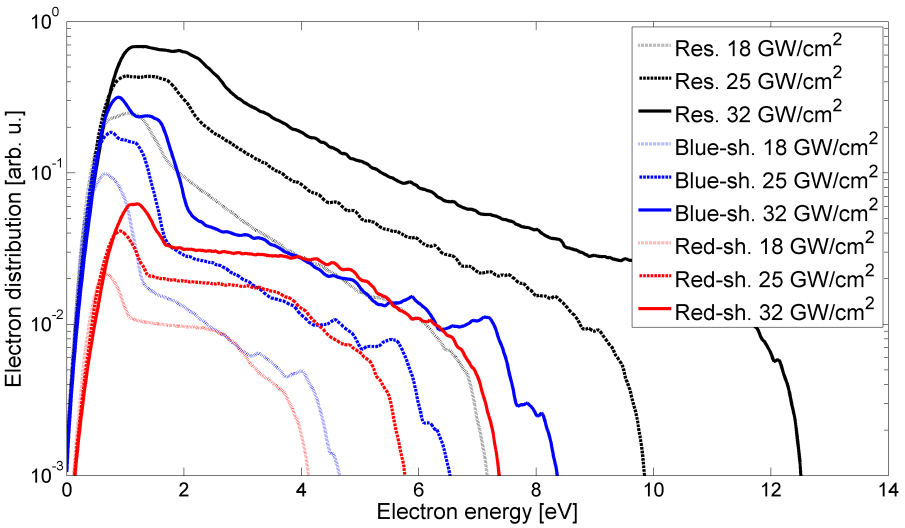

Figure 6.8.: Electron spectra for resonant and off-resonant rectangular particles.

6.4.3. Resonant and off-resonant case

We analyze in figure 6.1 analyzed off-resonant and resonant rectangular particles. The particle with dimensions 140x80x40 nm^3 is blue-shifted (resonance at 735 nm) and the particle with dimensions 180x80x40 nm^3 is red-shifted (resonance at λ =870 nm). Both particles were excited with the same plane wave excitation as the resonant particle at a wavelength of λ =800 nm. As the results in figure 6.8 show (see also figure 6.7 for results of the angle dependence for the off-resonant particles), the off-resonant particles have lower cut-off energies than the resonant one and a smaller number of emitted electrons. Both effects are due to the smaller field-enhancement than in the resonant case, which follows from the fact that the exciting field can not couple that strongly to the electron gas. A phase shift of 180 degrees for the blue shifted particle and a phase shift of zero degrees for the red-shifted particle in comparison with the exciting field is also observed, whereas the phase-shift for resonant ones is 90 degrees.

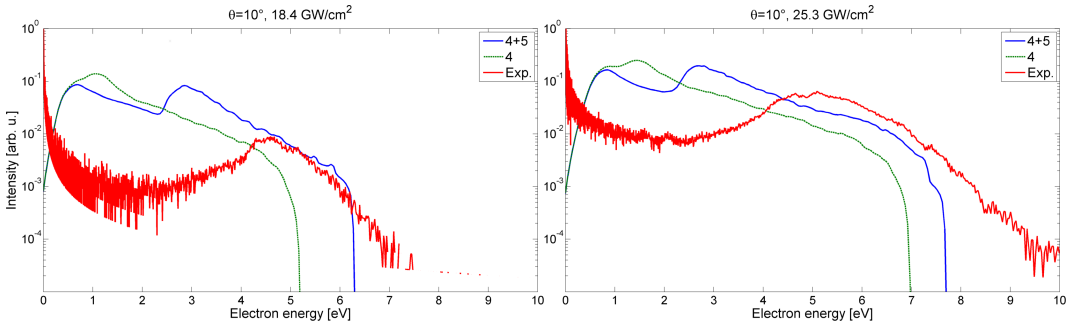

Figure 6.9.: Electron distribution with (4+5) and without (4) five-photon emission in comparison with experimental data from the group of Peter Dombi. (In the range from zero to 3 eV the experimental data are not very accurate due to measurement uncertainties.)

6.5. Simulation vs. experiment

The simulations under study were done in association with an experiment by the group of Peter Dombi from the Research Inst. for Solid-State Physics and Optics, Budapest. So we are able to compare our model with experimental findings.

The particle spectra are well reproduced by the simulation with the boundary element method. The results also show that the cut-off energies of hot electrons for the resonant case are in very good agreement with the experimental ones as can be seen from figure 6.10. Also the off-resonant particles and the bowtie particle show good agreement with experiment.

A comparison of the electron distribution (figure 6.9) suggests that a further process is involved which is responsible for the peak around 4-6 eV. A possible explanation is that above threshold ionization or additional kinetic electron energy at the starting point caused by the plasmon is shifting the electrons in this range to higher kinetic energies. The simulation with five photon emission included is pointing into this direction. Here, we give the electrons at initial field strengths between 9 V/nm and 14 V/nm a starting velocity of 2.5 eV, which accounts for the additional absorbed photon. These electrons then accelerate to higher final kinetic energies and produce a peak at 3 eV.

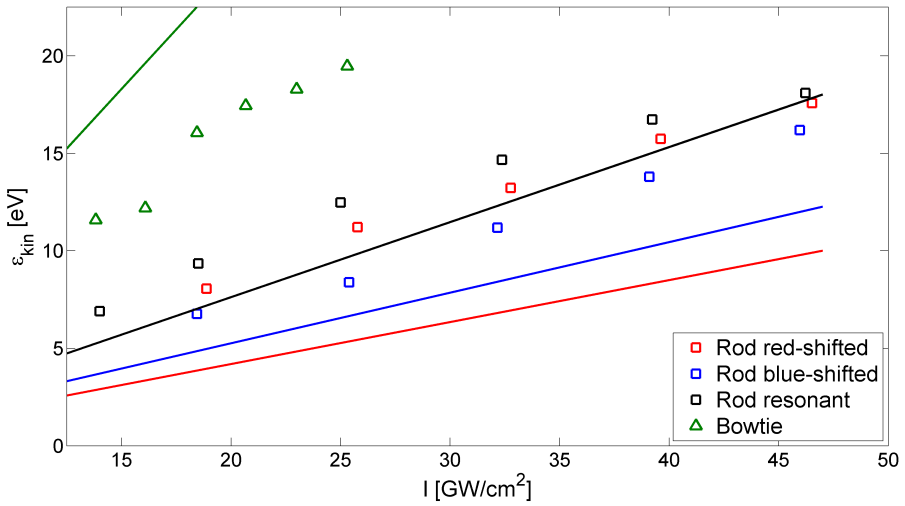

Figure 6.10.: Cut-off energies of different on- and off resonant particles with an excitation wavelength $\lambda = 800$ nm. Lines are simulated results and colors correspond to color of data points.

6.6. Conclusion and Outlook

In this thesis we studied electron emission from metallic nanoparticles. We used the so-called simple-man's model in order to describe the process. The electric fields where computed with the MNPBEM-Toolbox [15]. In particular we investigated the electron emission behavior of two different geometries: rectangular particles and bowtie antennas. In order to verify our model, we compared the simulation-results with measured electron spectra from lithographically fabricated gold nanoparticles with the same resonances, and found good agreement. Further simulations not shown in this thesis show that even better results can be obtained, if electron scattering is taken into account. This effect - observed at phases from about 90 degree to 180 degree - occurs, when the electron is first accelerated away from the particle, slows down, and then accelerates back to the particle, where it scatters elastically at the particle surface. The simulation results could also benefit from a more sophisticated model of the electron emission probability from metal surfaces. In detail, we found that the emission probability at high field strengths is underestimated. So a more thorough analysis for the emission probability should be done.

In future, the same model can be used e.g. to study different geometries and

radiation from the accelerated electrons.

7. Acknowledgements

I want to thank Ulrich Hohenester for guiding me through the whole process of creating this thesis. He had always an open door and good advice for me. Acknowledgements also goes to the Nanooptics/Optics and Laser science group from the University of Graz especially Univ. Prof. Joachim Krenn and Peter Dombi from the Research Inst. for Solid-State Physics and Optics, Budapest for very helpful discussions. Special thanks goes also to Jakob Ebner and Andreas Trügler for fruitful discussions and computational help. On a personal basis I want to thank Iri for her love and my family for their ongoing support and open doors at home through the years.

A. Appendix - Electromagnetic fields at surfaces

A.1. Boundary conditions for two media

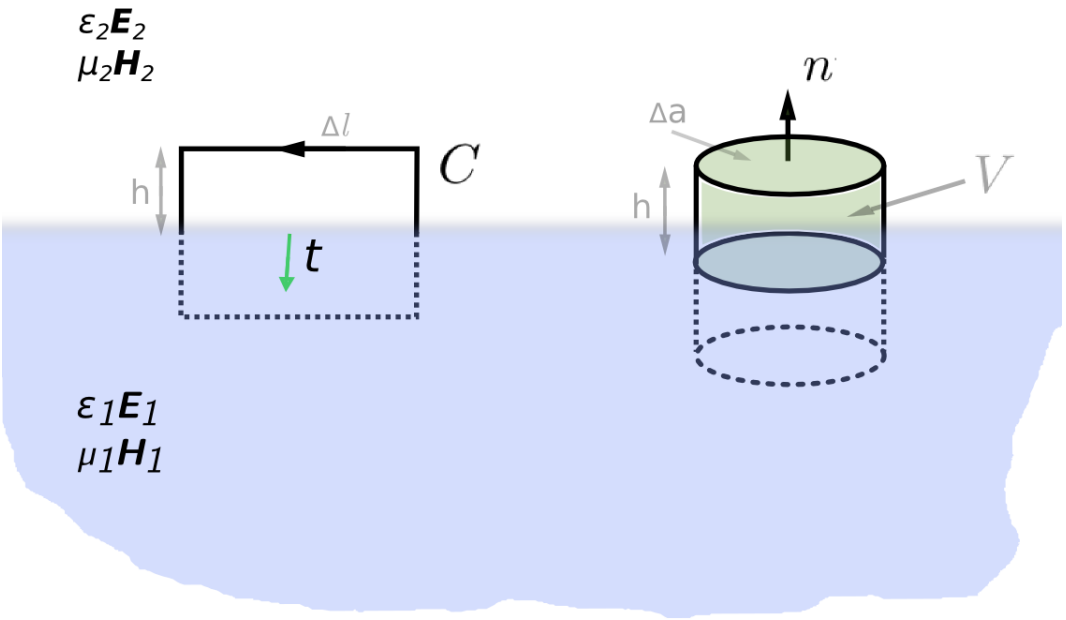

Figure A.1.: Interface between two media with different permittivity. The cylinder placed between the two media shows the volume V to be integrated for the boundary conditions of the normal components of the electromagnetic fields. By integrating Maxwell's equations over the contour C we get the tangential boundary conditions, where Δl lies parallel to the surface and the normal vector of the contourplane t is tangential to the surface of the interface.

To get the boundary conditions we write Maxwell's equations (3.1a) and

(3.1b) in the integral form [17]:

$$\oint_S \mathbf{D} \cdot \hat{\mathbf{n}}\, da = 4\pi \int_V \rho d^3x, \tag{A.1a}$$

$$\oint_S \mathbf{B} \cdot \hat{\mathbf{n}}\, da = 0. \tag{A.1b}$$

If we apply these integral equations to an appropriate volume V with an infinitesimal height h as shown in figure A.1 equations (A.1a) and (A.1b) are transformed to

$$\oint_S \mathbf{D} \cdot \hat{\mathbf{n}}\, da = (\mathbf{D}_2 - \mathbf{D}_1) \cdot \hat{\mathbf{n}}\, \Delta a,$$

$$\oint_S \mathbf{B} \cdot \hat{\mathbf{n}}\, da = (\mathbf{B}_2 - \mathbf{B}_1) \cdot \hat{\mathbf{n}}\, \Delta a.$$

The integral on the right in (A.1a) takes the form

$$4\pi \int_V \rho d^3x = 4\pi\sigma\Delta a.$$

So we obtain for the normal components of $\mathbf{D}$ and $\mathbf{B}$

$$(\mathbf{D}_2 - \mathbf{D}_1) \cdot \hat{\mathbf{n}} = 4\pi\sigma, \tag{A.2a}$$

$$(\mathbf{B}_2 - \mathbf{B}_1) \cdot \hat{\mathbf{n}} = 0, \tag{A.2b}$$

stating that the normal component of $\mathbf{B}$ is continuous at the interface and the normal component of $\mathbf{D}$ is discontinuous and equal to the surface charge density σ at the point of the volume.

A similar procedure leads to the tangential boundary conditions. We evaluate the integral form of (3.1c) and (3.1d) for the contour C with an infinitesimal height h

$$\oint_C \mathbf{H} \cdot d\mathbf{l} = \frac{1}{c} \int_{S'} \left(4\pi\mathbf{J} + \frac{\partial \mathbf{D}}{\partial t} \right) \cdot \hat{\mathbf{n}}\, da, \tag{A.3a}$$

$$\oint_C \mathbf{E} \cdot d\mathbf{l} = -\frac{1}{c} \int_{S'} \frac{\partial \mathbf{B}}{\partial t} \cdot \hat{\mathbf{n}}\, da, \tag{A.3b}$$

which leads to

$$\hat{\mathbf{n}} \times (\mathbf{E}_2 - \mathbf{E}_1) = 0, \tag{A.4a}$$

$$\hat{\mathbf{n}} \times (\mathbf{H}_2 - \mathbf{H}_1) = \mathbf{j}. \tag{A.4b}$$

This means that the tangential component of $\mathbf{E}$ is continuous at the interface and the tangential component of $\mathbf{H}$ is discontinuous, with a difference at the interface given by the surface current density $\mathbf{j}$.

In the quasistatic regime we can write equation (A.2a) as

$$(\epsilon_1 \boldsymbol{\nabla}\Phi_1 - \epsilon_2 \boldsymbol{\nabla}\Phi_2) \cdot \hat{\mathbf{n}} = 0,$$

or in an equivalent fashion we get for the normal components of the potential

$$\epsilon_1 \frac{\partial \Phi_1}{\partial n} = \epsilon_2 \frac{\partial \Phi_2}{\partial n}, \tag{A.5}$$

where $\frac{\partial \Phi_i}{\partial n} = \hat{\mathbf{n}} \cdot \boldsymbol{\nabla}\Phi_i$ is the surface derivative of the potential at a certain point of the interface. For the tangential components we arrive at

$$(\boldsymbol{\nabla}\Phi_1)^{\parallel} = (\boldsymbol{\nabla}\Phi_2)^{\parallel}. \tag{A.6}$$

A.2. Conversion from nm to eV

The photon energy in eV is given by the equation

$$E = \hbar\omega = \hbar c k = \hbar c \frac{2\pi}{\lambda}, \tag{A.7}$$

where ω is the frequency, k is the wavevector and λ is the wavelength in nm. The two constants, c the speed of light and Planck's reduced constant $\hbar$, take in SI-units the values [32]

$$\hbar = 6.58211899 \times 10^{-16} \text{ eVs}, \tag{A.8}$$

$$c = 2.99792458 \times 10^{8} \text{ m/s}. \tag{A.9}$$

Inserting in equation (A.7) we find for the conversion factor between eV and nm

$$E[\text{eV}] = \frac{\hbar 2\pi c}{\lambda} = \frac{1239.8}{2\pi} k \ [\text{nm}^{-1}] \ = \frac{1239.8}{\lambda} \ [\text{nm}^{-1}] \ . \tag{A.10}$$

For example the value of a wavelength of 800 nm corresponds to 1.55 eV (see figure A.2).

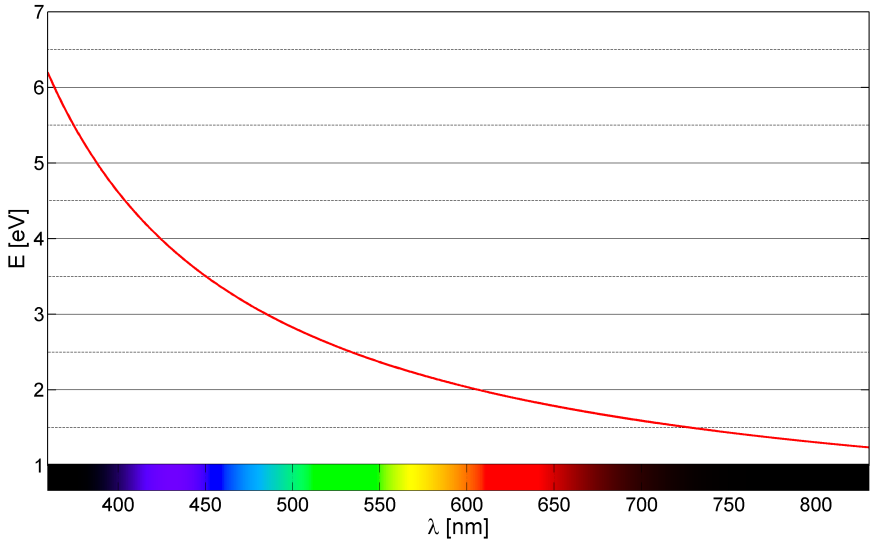

Figure A.2.: Conversion between nm and eV. The x-axis shows the visible wavelength spectrum.

A.3. Conversion from V/nm to GW/cm^2

Below we compute the conversion factor between the electric field strength E given in units of V/m and the power S given in W/m^2.

As we know [17], the pointing vector **S**, which gives the power density of the electromagnetic field is defined as

$$\mathbf{S} = \mathbf{E} \times \mathbf{H}. \tag{A.11}$$

Let us assume a sinusoidal plane wave propagating in z-direction, which is described by

$$\mathbf{E}(z,t) = E_x \cos(\omega t - k_z z), \tag{A.12}$$

$$\mathbf{H}(z,t) = H_y \cos(\omega t - k_z z). \tag{A.13}$$

As we know from Maxwell's equations in vacuum the electromagnetic field has to obey

$$\boldsymbol{\nabla} \times \mathbf{E} = -\mu \frac{\partial \mathbf{H}}{\partial t}. \tag{A.14}$$

For the sinusoidal plane wave the derivation of the left and right hand side

yield

$$\begin{aligned}\boldsymbol{\nabla} \times \mathbf{E} &= -k_z E_x \sin(\omega t - k_z z),\\ -\mu \frac{\partial \mathbf{H}}{\partial t} &= -\mu\omega H_y \sin(\omega t - k_z z).\end{aligned}$$

Inserted into equation (A.14), this gives a relation for the electric and magnetic amplitude, which reads

$$H_y = \frac{k_z}{\mu\omega} E_x = \frac{1}{\mu\omega c} E_x = \frac{1}{\mu}\sqrt{\epsilon\mu} E_x = \sqrt{\frac{\epsilon}{\mu}} E_x. \tag{A.15}$$

With the found relation we are now ready to obtain the power density for the electric field strength in vacuum:

$$\mathbf{S} = \sqrt{\frac{\epsilon}{\mu}} E_x^2 \cos^2(\omega t - k_z z). \tag{A.16}$$

The time averaged power is then

$$\overline{\mathbf{S}} = \frac{1}{\tau} \int_0^\tau dt \sqrt{\frac{\epsilon}{\mu}} E_x^2 \cos^2(\omega t - k_z z), \tag{A.17}$$

$$= \frac{1}{2}\sqrt{\frac{\epsilon}{\mu}} E_x^2, \tag{A.18}$$

where $\tau = 1/\nu$ is the time of oscillation. We call $Z_0 = 1/\sqrt{\frac{\epsilon}{\mu}}$ the impedance of the medium, which is in vacuum $Z_0 = 1/377$. So we get as a conversion factor between $\mathrm{W/m^2}$ and V/m

$$\overline{\mathbf{S}}\ [\mathrm{W/m^2}] \ = \frac{1}{2 \times 377} (E_x\ [\mathrm{V/m}])^2. \tag{A.19}$$

Here, E_x is the maximum electric field amplitude and not the effective field amplitude. A more commonly used conversion is between V/nm and $\mathrm{GW/cm^2}$, which is given by

$$\overline{\mathbf{S}}\ [\mathrm{GW/cm^2}] \ = \frac{1}{2 \times 377} 10^5 (E_x\ [\mathrm{V/nm}])^2. \tag{A.20}$$

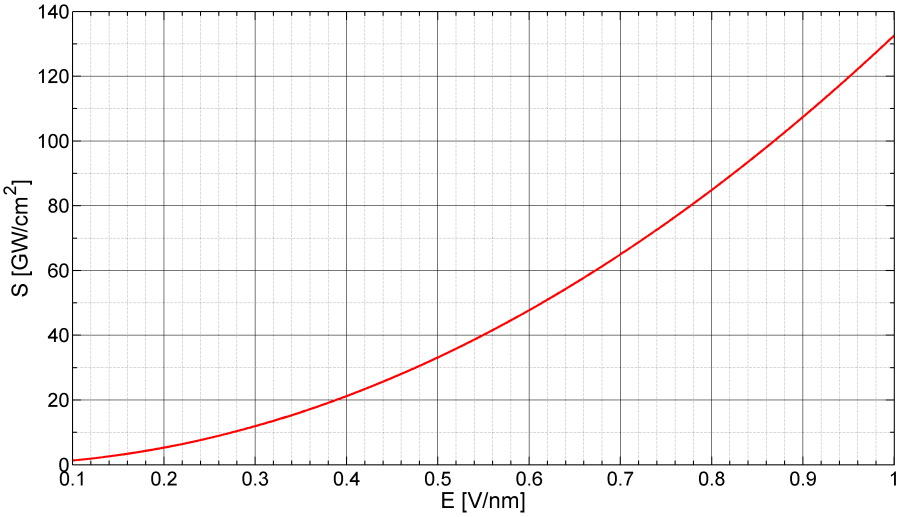

Figure A.3.: Conversion between GW/cm^2 and V/nm. As impedance the value of vacuum $Z_0 = 377$ is used.

B. Appendix - Nonlinear photoionization

B.1. Wentzel-Kramer-Brillouin Approximation

We want to derive the transmission amplitude of a particle going through a barrier. To do so we use the Wentzel-Kramer-Brillouin approximation [30]. A similar derivation is accomplished e.g. in [12] or [11]. Other derivations are found e.g. in [22] or also in [12]. We rewrite the Schrödinger equation

$$\left(-\frac{\hbar}{2m}\frac{d^2}{dx^2}+V(x)\right)\Psi(x)=\epsilon\Psi(x), \tag{B.1}$$

in the form

$$\frac{d^2\Psi}{dx^2}=-\frac{p(x)^2}{\hbar^2}\Psi, \tag{B.2}$$

where $p(x)=\sqrt{2m(\epsilon-V(x))}$ is the classical momentum of a particle with total energy ϵ. Without loss of generality we assume a solution for the wave-function Ψ in terms of the complex function $S(x)$ in the form of

$$\Psi(x)=\mathrm{e}^{iS(x)/\hbar}\,. \tag{B.3}$$

We insert the solution into equation (B.2) and find (note that we have dropped the x-dependence in $S(x)$)

$$\frac{d\Psi}{dx}=\frac{i}{\hbar}S'\,\mathrm{e}^{iS/\hbar}, \tag{B.4}$$

$$\frac{d^2\Psi}{dx^2}=\left(\frac{i}{\hbar}S''-\frac{1}{\hbar^2}(S')^2\right)\mathrm{e}^{iS/\hbar}\,. \tag{B.5}$$

Equation (B.2) yields

$$\left(\frac{i}{\hbar}S''-\frac{1}{\hbar^2}(S')^2\right)\mathrm{e}^{iS/\hbar}=-\frac{p(x)^2}{\hbar^2}\,\mathrm{e}^{iS/\hbar}\Rightarrow \tag{B.6}$$

$$i\hbar S''-(S')^2+p^2=0. \tag{B.7}$$

Now we are free to expand $S(x)$ in a power series in $\hbar$

$$S(x) = S_0(x) + \hbar S_1(x) + \hbar^2 S_2(x) + \dots \tag{B.8}$$

By implementing (B.8) into (B.2) and collecting powers of $\hbar$ we find

$$-(S_0')^2 + p^2 + \hbar(iS_0'' - 2S_0'S_1') + \hbar^2(iS_1'' - 2S_0'S_2' + (S_1')^2) + \dots = 0. \tag{B.9}$$

and therefore

$$(S_0')^2 = p^2,\ iS_0'' = 2S_0'S_1' \text{ and } iS_1'' - 2S_0'S_2' = -(S_1')^2. \tag{B.10}$$

So, by integrating and inserting we find in first order of $\hbar$

$$S_0 = \pm \int p(x)dx + const., \tag{B.11}$$

$$S_1 = \frac{i}{2}\ln p + const. \tag{B.12}$$

We write the solution of (B.2) in first order of S as

$$\Psi = \mathrm{e}^{S_0+S_1} = \frac{C}{\sqrt{p}}\exp\left(\pm\int p dx\right). \tag{B.13}$$

Let us consider now an energy barrier between the classical turning points x_1 and x_2. Then we get an incoming wave Ψ_1 for $x < x_1$ and an outgoing wave Ψ_2 for $x > x_2$:

$$\Psi_1(x < x_1) \propto \exp\left(\int_{-\infty}^{x_1} p dx\right), \tag{B.14}$$

$$\Psi_2(x > x_2) \propto \exp\left(\int_{x_2}^{\infty} p dx\right). \tag{B.15}$$

Inserting p again the transmission probability reads

$$T(\epsilon) = \left|\frac{\Psi_2}{\Psi_1}\right|^2 = \left|\frac{\exp\left(\int_{-\infty}^{x_1} p dx\right)}{\exp\left(\int_{x_2}^{\infty} p dx\right)}\right|^2, \tag{B.16}$$

$$= \exp\left(\frac{-2}{\hbar}\int_{x_1}^{x_2}\sqrt{2m(V(x)-\epsilon)}dx\right) \tag{B.17}$$

B.2. Derivation of Multiphoton emission

B.2.1. Two photon emission

We begin with equation (4.11)

$$i\frac{da_m^N}{dt} = \sum_l a_l^{N-1}(t) V_{ml}\, \mathrm{e}^{-i\omega_{lm}t}, \tag{B.18}$$

and solve it for N=1, and N=2. The result for N=1, was already obtained in subsection 4.1, equation (4.14), and we again drop the second term which describes photon emission and only retain the first one:

$$a_m^1(t) = \frac{\mu_{mg}E}{\hbar(\omega_{mg}-\omega)}\left[\mathrm{e}^{i(\omega_{mg}-\omega)t}-1\right]. \tag{B.19}$$

For the potential between the transition states we again use the rotating wave approximation and define the interaction as

$$V_{nm} = -\mu_{nm}\left(E\,\mathrm{e}^{-i\omega t}+E^*\,\mathrm{e}^{i\omega t}\right), \tag{B.20}$$

$$\cong -\mu_{nm}\left(E\,\mathrm{e}^{-i\omega t}\right). \tag{B.21}$$

Now we are ready to evaluate equation (B.18) by inserting equations (B.19) and (B.21), which gives in the case of N=2 the transition amplitude for the two photon absorption:

$$\frac{d}{dt}a_n^2(t) = (i\hbar)^{-1}\sum_m a_m^1(t) V_{nm}\,\mathrm{e}^{-i\omega_{mn}t} \tag{B.22}$$

$$= (i\hbar)^{-1}\sum_m \frac{\mu_{nm}\mu_{mg}E^2}{\hbar(\omega_{mg}-\omega)}\left(\mathrm{e}^{i(\omega_{mg}-2\omega)t}-\mathrm{e}^{i(\omega_{nm}-\omega)t}\right). \tag{B.23}$$

Now we are free to drop the term $\mathrm{e}^{i(\omega_{nm}-\omega)t}$, which accounts for the transient response of the system and does not affect two photon absorption. By integration we directly obtain the solution for the two-photon transition amplitude

$$a_n^2(t) = (i\hbar)^{-1}\sum_m \frac{\mu_{nm}\mu_{mg}E^2}{\hbar(\omega_{mg}-\omega)}\left(\frac{\mathrm{e}^{i(\omega_{mg}-2\omega)t}-1}{\omega_{ng}-2\omega}\right). \tag{B.24}$$

Now we proceed in the same way as for the one-photon absorption, that is we calculate the probability for two-photon absorption by taking the square of the

transition amplitude

$$p_n^2(t) = |a_n^2(t)|^2 = \left|(i\hbar)^{-1}\sum_m \frac{\mu_{nm}\mu_{mg}E^2}{\hbar(\omega_{mg}-\omega)}\right|^2 \left|\left(\frac{\mathrm{e}^{i(\omega_{mg}-2\omega)t}-1}{\omega_{ng}-2\omega}\right)\right|^2 \tag{B.25}$$

and for large times we arrive again at a Dirac-delta function for the second term:

$$p_n^2(t) = \left|(i\hbar)^{-1}\sum_m \frac{\mu_{nm}\mu_{mg}E^2}{\hbar(\omega_{mg}-\omega)}\right|^2 2\pi t\delta(\omega_{ng}-2\omega). \tag{B.26}$$

As the probability is seen to increase with time, we define a probability per unit time

$$P_{ng}^2 = \frac{p_n^2(t)}{t}. \tag{B.27}$$

Finally multiplying the probability per unit time with the number of states dm and integrating over the density of states in the continuum as done in equation (4.19) we arrive at an solution for the transition probability per unit time

$$P_{ng}^2 = \left|(i\hbar)^{-1}\sum_m \frac{\mu_{nm}\mu_{mg}E^2}{\hbar(\omega_{mg}-\omega)}\right|^2 2\pi\delta(\omega_{ng}-2\omega). \tag{B.28}$$

This result can be again recast into a formulation dependent on the intensity $I = 2n\epsilon_0 c|E|^2$ of the electric field and an absorption cross section $\sigma_{ng}^2(\omega)$ leading to

$$P_n^2 = \sigma_{ng}^2(\omega)I^2, \tag{B.29}$$

$$\sigma_{ng}^2(\omega) = \frac{\pi}{2n^2\epsilon_0^2c^2}\left|\sum_m \frac{\mu_{nm}\mu_{mg}}{\hbar^2(\omega_{mg}-\omega)}\right|^2 \rho_n\big|_{\omega_{ng}=2\omega}. \tag{B.30}$$

Bibliography

[1] M. V. Ammosov, N. B. Delone, and V. P. Krainov. Tunnel ionization of complex atoms and atomic ions by an alternating electromagnetic field. *Soviet Physics JETP*, 64:1191, Nov. 1986.

[2] H. A. Atwater. The promise of plasmonics. *SIGDA Newsl.*, 37(9):1:1–1:1, May 2007.

[3] R. Boyd. *Nonlinear Optics*. Academic Press. Academic Press, 2008.

[4] P. B. Corkum. Plasma perspective on strong field multiphoton ionization. *Phys. Rev. Lett.*, 71:1994–1997, Sep 1993.

[5] N. Delone and V. Krainov. *Multiphoton Processes in Atoms*. Springer Series on Atoms + Plasmas. Springer, 2000.

[6] N. B. Delone and V. P. Krainov. *Atoms in strong light fields / N.B. Delone, V.P. Krainov ; [translator, Eugeny M. Yankovsky]*. Springer-Verlag, Berlin ; New York :, 1985.

[7] P. Dombi and P. Rácz. Ultrafast monoenergetic electron source by optical waveform control of surface plasmons. *Opt. Express*, 16(5):2887–2893, Mar 2008.

[8] A. Einstein. über einen die erzeugung und verwandlung des lichtes betreffenden heuristischen gesichtspunkt. *Annalen der Physik*, 322(6):132–148, 1905.

[9] R. H. Fowler and L. Nordheim. Electron emission in intense electric fields. *Proceedings of the Royal Society of London. Series A*, 119(781):173–181, 1928.

[10] F. J. García de Abajo and A. Howie. Retarded field calculation of electron energy loss in inhomogeneous dielectrics. *Phys. Rev. B*, 65:115418, Mar 2002.

[11] A. Gehring. *Simulation of Tunneling in Semiconductor Devices*. PhD thesis, Technische Universität Wien, 2003.

[12] D. Griffiths. *Introduction to Quantum Mechanics*. Prentice Hall International Editions. Prentice Hall, 1994.

[13] G. Herink, D. R. Solli, M. Gulde, and C. Ropers. Field-driven photoemission from nanostructures quenches the quiver motion. *Nature*, 483(7388):190–193, Mar. 2012.

[14] U. Hohenester and J. Krenn. Surface plasmon resonances of single and coupled metallic nanoparticles: A boundary integral method approach. *Phys. Rev. B*, 72:195429, Nov 2005.

[15] U. Hohenester and A. Trügler. MNPBEM - a matlab toolbox for the simulation of plasmonic nanoparticles. *Comp. Phys. Commun.*, 183, 2012.

[16] U. Hohenester and A. Trügler. *Optical Properties of Metallic Nanoparticles: Introduction and Basic Principles*. Springer, 2012.

[17] J. D. Jackson. *Classical Electrodynamics Third Edition*, volume 67. Wiley, 1998.

[18] L. V. Keldysh. Ionization in the field of a strong electromagnetic wave. *Soviet Physics JETP*, 20:1307–1314, May 1965.

[19] M. Krüger, M. Schenk, and P. Hommelhoff. Attosecond control of electrons emitted from a nanoscale metal tip. *Nature*, 475(7354):78–81, July 2011.

[20] L. Lorenz. On the identity of the vibrations of light with electrical currents. *Philos. Mag. 34*, pages 287–301, 1867.

[21] J. C. Maxwell. A dynamical theory of the electromagnetic field. *Philosophical Transactions of the Royal Society of London*, 155:459–513, 1865.

[22] A. Messiah. *Messiah, Albert: Quantenmechanik*. Quantenmechanik. De Gruyter, 1990.

[23] G. Mie. Beiträge zur optik trüber medien, speziell kolloidaler metallösungen. *Annalen der Physik*, 330(3):377–445, 1908.

[24] K. Mishima, M. Hayashi, J. Yi, S. H. Lin, H. L. Selzle, and E. W. Schlag. Generalization of keldysh's theory. *Phys. Rev. A*, 66:033401, Sep 2002.

[25] L. Novotny and B. Hecht. *Principles of Nano-Optics*. Cambridge University Press, 2006.

[26] E. Palik. *Handbook of Optical Constants of Solids Five-volume Set: Handbook of optical constants of solids I, II, & III*. Handbook of Optical Constants of Solids Five-volume Set. Academic Press, 1998.

[27] A. M. Perelomov, V. S. Popov, and M. V. Terent'ev. Ionization of Atoms in an Alternating Electric Field. *Soviet Journal of Experimental and Theoretical Physics*, 23:924, Nov. 1966.

[28] M. Schenk, M. Krüger, and P. Hommelhoff. Strong-field above-threshold photoemission from sharp metal tips. *Phys. Rev. Lett.*, 105:257601, Dec 2010.

[29] L. Verlet. Computer "experiments" on classical fluids. i. thermodynamical properties of lennard-jones molecules. *Phys. Rev.*, 159:98–103, Jul 1967.

[30] G. Wentzel. Eine verallgemeinerung der quantenbedingungen für die zwecke der wellenmechanik. *Zeitschrift für Physik A Hadrons and Nuclei*, 38:518–529, 1926. 10.1007/BF01397171.

[31] S. V. Yalunin, M. Gulde, and C. Ropers. Strong-field photoemission from surfaces: Theoretical approaches. *Phys. Rev. B*, 84:195426, Nov 2011.

[32] W.-M. Yao, C. Amsler, D. Asner, R. Barnett, J. Beringer, P. Burchat, C. Carone, C. Caso, O. Dahl, G. D'Ambrosio, A. DeGouvea, M. Doser, S. Eidelman, J. Feng, T. Gherghetta, M. Goodman, C. Grab, D. Groom, A. Gurtu, K. Hagiwara, K. Hayes, J. Hernández-Rey, K. Hikasa, H. Jawahery, C. Kolda, K. Y., M. Mangano, A. Manohar, A. Masoni, R. Miquel, K. Mönig, H. Murayama, K. Nakamura, S. Navas, K. Olive, L. Pape,

C. Patrignani, A. Piepke, G. Punzi, G. Raffelt, J. Smith, M. Tanabashi, J. Terning, N. Törnqvist, T. Trippe, P. Vogel, T. Watari, C. Wohl, R. Workman, P. Zyla, B. Armstrong, G. Harper, V. Lugovsky, P. Schaffner, M. Artuso, K. Babu, H. Band, E. Barberio, M. Battaglia, H. Bichsel, O. Biebel, P. Bloch, E. Blucher, R. Cahn, D. Casper, A. Cattai, A. Ceccucci, D. Chakraborty, R. Chivukula, G. Cowan, T. Damour, T. DeGrand, K. Desler, M. Dobbs, M. Drees, A. Edwards, D. Edwards, V. Elvira, J. Erler, V. Ezhela, W. Fetscher, B. Fields, B. Foster, D. Froidevaux, T. Gaisser, L. Garren, H.-J. Gerber, G. Gerbier, L. Gibbons, F. Gilman, G. Giudice, A. Gritsan, M. Grünewald, H. Haber, C. Hagmann, I. Hinchliffe, A. Höcker, P. Igo-Kemenes, J. Jackson, K. Johnson, D. Karlen, B. Kayser, D. Kirkby, S. Klein, K. Kleinknecht, I. Knowles, R. Kowalewski, P. Kreitz, B. Krusche, Y. Kuyanov, O. Lahav, P. Langacker, A. Liddle, Z. Ligeti, T. Liss, L. Littenberg, L. Liu, K. Lugovsky, S. Lugovsky, T. Mannel, D. Manley, W. Marciano, A. Martin, D. Milstead, M. Narain, P. Nason, Y. Nir, J. Peacock, S. Prell, A. Quadt, S. Raby, B. Ratcliff, E. Razuvaev, B. Renk, P. Richardson, S. Roesler, G. Rolandi, M. Ronan, L. Rosenberg, C. Sachrajda, S. Sarkar, M. Schmitt, O. Schneider, D. Scott, T. Sjöstrand, G. Smoot, P. Sokolsky, S. Spanier, H. Spieler, A. Stahl, T. Stanev, R. Streitmatter, T. Sumiyoshi, N. Tkachenko, G. Trilling, G. Valencia, K. van Bibber, M. Vincter, D. Ward, B. Webber, J. Wells, M. Whalley, L. Wolfenstein, J. Womersley, C. Woody, A. Yamamoto, O. Zenin, J. Zhang, and R.-Y. Zhu. Review of Particle Physics. *Journal of Physics G*, 33:1+, 2006.

[33] G. L. Yudin and M. Y. Ivanov. Nonadiabatic tunnel ionization: Looking inside a laser cycle. *Phys. Rev. A*, 64:013409, Jun 2001.